COMPUTATIONAL METHODS FOR MESOSCOPIC, INHOMOGENEOUS PLASTIC DEFORMATION

Nasr M. Ghoniem
Mechanical and Aerospace Engineering Department
University of California, Los Angeles, CA 90095-1597, USA

October 21, 1999

Abstract

This article reviews and expands on recent research by the author on the development and applications of a new approach to the description of heterogeneuos plastic deformation in materials. The equations of motion of three-dimensional (3-D) interacting dislocation loops are developed on the basis of irreversible thermodynamics. Variational methods are utilized to obtain the specific forms of these equations. The method is aimed at facilitating large-scale computer simulations of inhomogeneous plastic deformation, and associated applications in pattern-forming plastic instabilities. Each dislocation segment is represented as a parametric space curve of specified smooth shape functions and Degrees of Freedom (DF) associated with beginning and end nodes. Kinetic equations for specific generalized coordinates describing dislocation motion are derived. For general climb/glide 3-D motion of a curved dislocation segment, the number of degrees of freedom $N_{DF} = 3n$, where $n = 1$ for linear; $n = 2$ for cubic; and $n = 3$ for quintic parametric splines, respectively. It is also shown that the position $\mathbf{P}$, tangent $\mathbf{T}$, and normal $\mathbf{N}$ vectors at segment nodes are sufficient to describe general 3-D dislocation motion. For constrained glide motion, however, we also show that only two degrees of freedom are adequate for determination of dislocation loop profiles, including crystal structure constraints. A fast sum method for determination of the elastic field of dislocation ensembles is developed and applied to determine displacements, strains, stresses, energies and forces associated with arbitrarily curved dislocation loops. A number of examples are given to illustrate the following features of the method: (1) adaptive node generation on interacting segments, (2) variable time-step determination for integration of the equations of motion, (3) dislocation generation by the Frank-Read mechanism in Face Center Cubic (fcc), Body Center Cubic (bcc) and Diamond Cubic (dc) crystals, (4) loop-loop deformation and interaction, (5) formation of dislocation junctions, and (6) dislocation microstructure evolution.

1 INTRODUCTION

A fundamental description of plastic deformation has been recently pursued in many parts of the world as a result of dissatisfaction with the limitations of continuum plasticity theory. Although continuum models of plastic deformation are extensively used in engineering practice, their range of application is limited by the underlying database. The

reliability of continuum plasticity descriptions is dependent on the accuracy and range of available experimental data. Under complex loading situations, however, the database is often hard to establish. Moreover, the lack of a characteristic length scale in continuum plasticity makes it difficult to predict the occurance of critical localized deformation zones. Although homogenization methods have played a significant role in determining the elastic properties of new materials from their constituents (e.g. composite materials), the same methods have failed to describe plasticity. It is widely appreciated that plastic strain is fundamentally heterogenous, displaying high strains concentrated in small material volumes, with virtually undeformed regions in-between. Experimental observations consistently show that plastic deformation is internally heterogeneous at a number of length-scales [1]- [4]. Depending on the deformation mode, heterogeneous dislocation structures appear with definitive wavelengths. It is common to observe Persistent Slip Bands (PSB's), shear bands, dislocation pile ups, dislocation cells and sub grains. However, a satisfactory description of realistic dislocation patterning and strain localization has been rather elusive. Attempts aimed at this question have been based on statistical mechanics [5]- [10], reaction-diffusion dynamics [11]- [13], or the theory of phase transitions [14]. Much of the efforts represented by Refs. [5]- [14] have aimed at clarifying the fundamental origins of inhomogeneous plastic deformation. On the other hand, engineering descriptions of plasticity have relied on experimentally verified constitutive equations.

Because the internal geometry of deforming crystals is very complex, a physically-based description of plastic deformation can be very challenging. The topological complexity is manifest in the existence of dislocation structures within otherwise perfect atomic arrangements. Dislocation loops delineate regions where large atomic displacements are encountered. As a result, long-range elastic fields are set up in response to such large, localized atomic displacements. As the external load is maintained, the material deforms plastically by generating more dislocations. Thus, macroscopically observed plastic deformation is a consequence of dislocation generation and motion. A closer examination of atomic positions associated with dislocations shows that large displacements are confined only to a small region around the dislocation line (i.e. *the dislocation core*). The majority of the displacement field can be conveniently described as elastic deformation. Even though one utilizes the concept of dislocation distributions to account for large displacements close to dislocation lines, a physically-based plasticity theory can paradoxically be based on the theory of elasticity!

The properties and interactions of simplified dislocation geometries have been the subject of intensive investigations for the past few decades ([15], [16]). The strength, mechanical, and some physical properties have been rationalized as a consequence of dislocation behavior in materials. Methods for evaluation of the elastic field of dislocations in materials are largely based on analytical solutions for special geometries of single dislocation lines, circular dislocation loops, or finite straight segments ([15], [16]). Interaction forces and energies between dislocations are also available in closed analytical form for simplified dislocation line geometries, which involve series summations over Bessel functions [17], or elliptic integrals ([18]- [21]).

A relatively recent approach to investigating the fundamental aspects of plastic deformation is based on direct numerical simulation of the interaction and motion of dislocations. This approach, which is commonly known as Dislocation Dynamics (DD), was first introduced for 2-D straight, infinitely long dislocation distributions [22] - [34], and then

later for complex 3-D microstructure [35] - [51]. In DD simulations of plastic deformation, the computational effort per time-step is proportional to the square of the number of interacting segments, because of the long-range stress field associated with dislocation lines. The computational requirements for 3-D simulations of plastic deformation of even single crystals are thus very challenging. It is therefore advantageous to reduce the total number of Equations Of Motion (EOM) during such calculations. Pioneering 3-D DD simulations of plasticity using straight segments are based on analytical solutions of the elastic field of pure screw and edge segments [35] - [45], or segments of mixed character [46]- [50]. Zbib, Rhee and Hirth [50] have shown that the length of each straight segment is roughly limited to $\sim 50 - 200$ units of Burgers vector. Longer segments may have substantial force variations, thus limiting the usefulness of one single equation of motion for the entire segment. While Fig. 1 shows a schematic representation for the position of displaced segments, Fig. 2 illustrates force distributions on them. Singular forces and stresses arise at sharp intersection points of straight segments, which result in divergence of the average force over the straight segment as the segment length is decreased, as can be seen schematically from Fig. 2. When the dislocation loop is discretized to only screw or edge components, which move on a crystallographic lattice [35] - [45], the accuracy of strong dislocation interactions is compromised because line curvatures are crudely calculated. In addition, motion of dislocation segments on a fixed lattice produces inherent limitations to the accuracy of the overall dislocation dynamics. Recently, Schwartz [47] - [49] developed an adaptive method to reduce the segment size when dislocation interactions become strong. Using a modified form of the Brown formula [52] for the self-force on a segment, the field divergence problem for very short segments was circumvented . For closely interacting dislocations, substantial curvature and re-configuration of dislocations occur during the formation of a junction, dipole, or other configuration [49]. However, the number of straight segments required to capture these processes is very large, and the segment size may have to be on the order of a few Burgers vectors. Most of these difficulties recognized from Figs. 1 and 2 arise from the linear segment approximation, the *differential* treatment for their equations of motion, and the required curvature approximation for the self-force.

The study of dislocation configurations at short-range can be quite complex, because of large deformations and reconfiguration of dislocation lines during their interaction. Thus, adaptive grid generation methods and more refined treatments of self-forces have been found to be necessary [47]- [49]. In some special cases, however, simpler topological configurations are encountered. For example, long straight dislocation segments are experimentally observed in materials with high Peierel's potential barriers (e.g. covalent materials), or when large mobility differences between screw and edge components exist (e.g. some BCC crystals at low temperature). Under conditions conducive to glide of small prismatic loops on glide cylinders, or the uniform expansion of nearly circular loops, changes in the loop *shape* is nearly minimal during its motion. Also, helical loops of nearly constant radius are sometimes observed in quenched or irradiated materials under the influence of point defect fluxes. It is clear that, depending on the particular application and physical situation, one would be interested in a flexible method which can capture the essential physics at a reasonable computational cost. A consequence of the long-range nature of the dislocation elastic field is that the computational effort per time step is proportional to the square of the number of interacting segments. It is therefore advantageous to reduce the number of interacting segments within a given computer simulation, or to

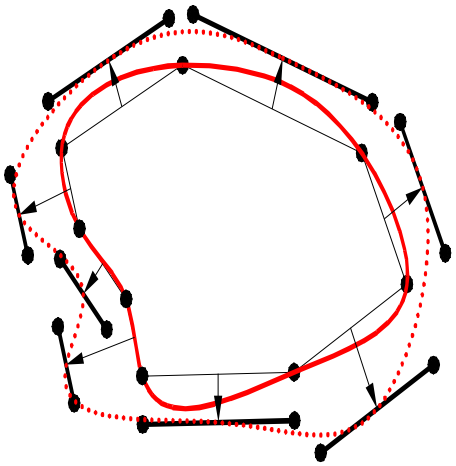

Figure 1: Discretization of a dislocation loop with linear segments leads to loss of connectivity when the equations of motion are developed only for mid-points.

develop more efficient approaches to computations of the long range field ([26], [31], [50]).

Dislocation loops in DD computer simulations are treated as dynamical systems, which can be described by the time dependence of specified coordinates. Obviously, if one attempts to solve the equations of dynamics for each atom within and surrounding the dislocation core, the number of equations is prohibitively large. On the other hand, if one knows that certain modes of motion for groups of atoms are closely-linked, many equations can be *adiabatically* eliminated, as is now conventional in the treatment of dynamical systems. Thus, instead of developing equations for the geometry of each single atom, one can find a much smaller set of geometric *generalized coordinates*, which would adequately describe the dynamical behavior of an entire dislocation loop. In Lagrangian descriptions, a number of generalized coordinates, q_r, is selected, where the subscript r represents a specific *Degree of Freedom (DF)* for the dynamical system. In a numerical computer simulation, however, the size of the system depends on available N_{DF}. Within the context of DD, one would expect that N_{DF} is relatively small in loops which conform to specific crystallographic or mobility constraints, while N_{DF} can be somewhat large in situations where strong interactions, cross-slip, or similar processes take place. In general, it is not of interest to follow every wiggle and bump on dislocation lines, unless such details develop into full-fledged instabilities. For specific applications, however, we intend to reduce N_{DF} as much as reasonable for the description of the physical situation at hand. This will be clarified by a number of examples, where physical constraints are imposed on dislocation motion.

Our plan here is to describe the equations of motion for generalized coordinates in much the same way as in Lagrangian mechanics. Regardless of the dislocation loop shape complexity, we will develop an *integral* equation of motion for each curved segment within the loop, such that only relationships between global thermodynamic variables are obeyed. For concreteness, we focus the current approach on dislocation line representation by parametric dislocation segments, similar to the Finite Element Method (FEM). Thus, the equations of motion for the transport of atoms within the dislocation core should be

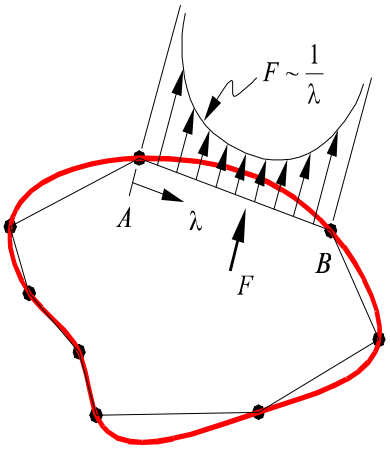

Figure 2: Force distribution on the straight segment AB from neighboring segments shows singular behavior at sharp corners. Force averaging over linear segments diverges as its length is decreased.

consistent with the thermodynamics of irreversibility. A challenging prospect in such a description is the enormous topological complexity of materials containing dislocations. Dislocation lines assume complex shapes, particularly during heavy deformation and at high temperatures where they execute truly 3-D motion as a result of combined glide and climb forces. These dislocations can be highly curved because of their strong mutual interactions, externally applied stress fields, as well as other thermodynamic forces. It is apparent that whenever large curvature variations are expected, the accuracy of computing the dynamic shape of dislocation loops becomes critical.

The motivation behind the current work can be stated as follows:

1. To reduce the computational burden by providing a high degree of flexibility in the selection of *both length and shape* of a dislocation segment.

2. To avoid numerical problems arising from singularities at intersecting straight segments.

3. To calculate the self-force on dislocation segments with a high degree of accuracy.

4. To provide a flexible tool which sheds more light on the physics of close-range interactions involving in-plane high curvature variations.

5. To effectively deal with the physics of climb and cross-slip, which require out-of-plane dislocation line curvature.

Although the theoretical foundations of dislocation theory are well-established (e.g. [15], [16], [53]- [54]), efficient computational methods are still in a state of development (e.g. [39], [50], [55]- [57]). Other than a few cases of perfect symmetry and special conditions ([18], [19], [17],), the elastic field of 3-D dislocations of arbitrary geometry is not analytically available. The field of dislocation ensembles is likewise analytically

unattainable. We plan, therefore, to present the main elements of 3-D dislocation theory such that the restrictions and limitations of the present computational method are clarified. The main steps in deriving equations for all field variables will thus be given, while the interested reader can find more helpful details in references ([21], [54], [57]).

The article is organized as follows. First, a brief review of experimental observations on inhomogeneous plastic deformation is given in Sec. 2. This is followed by a discussion of irreversible thermodynamics of dislocation motion in Sec. 3, in which we discuss energy components and entropy production during loop motion. This leads to an integral form of the variation in Gibbs energy in Sec. 4. A *weak* form of a variational procedure is pursued to formulate the equations of motion for the degrees of freedom based on the Galerkin approach. Differential geometry of complex dislocation loops, as well as associated computational protocols which are used to handle close-range interactions are then discussed in Sec. 5. In Sec. 6, we present a self-sufficient outline of a calculation procedure for the elastic field variables (e.g. displacement, strain, stress, energy and forces) for complex-shape dislocation loops. Several test cases for verification of the fast sum method are then given in Sec. 7. We compare calculation results for the stress field and energies of dislocation loops with those of known analytical and numerical solutions. Computer simulations of several problems of loop-loop interaction and dislocation generation in fcc, bcc and diamond cubic (dc) Si crystals are given in Sec. 8 . Finally, conclusions and discussions follow in Sec. 9.

2 EXPERIMENTAL EVIDENCE OF INHOMOGENEOUS PLASTIC DEFORMATION

Plastic deformation of materials has been observed to be heterogeneous at several length scales. At the macroscopic level, shear bands are known to localize plastic strain, leading to material failure. At smaller length scales, dislocation distributions are mostly heterogeneous in deformed materials, leading to the formation of a number of strain patterns ([1], [58] - [62]). Generally, dislocation patterns are thought to be associated with energy minimization of the deforming material, and manifest themselves as regions of high dislocation density separated by zones of virtually undeformed material. Dislocation-rich regions are zones of facilitated deformation, while dislocation poor regions are hard spots in the material, where plastic deformation does not occur [63]. Dislocation structures, such as Persistent slip Bands (PSB's), planar arrays, dislocation cells, and subgrains, are experimentally observed in metals under both cyclic and steady deformation conditions [64]. Persistent slip bands are formed under cyclic deformation conditions, and have been mostly observed in copper and copper alloys [60], [65], [66]. They appear as sets of parallel walls composed of dislocation dipoles, separated by dislocation-free regions. The length dimension of the wall is orthogonal to the direction of dislocation glide. Fig. 3 shows a TEM picture of experimental observations of PSB's.

Dislocation planar arrays are formed under monotonic stress deformation conditions, and are composed of parallel sets of dislocation dipoles, as shown in Fig. 4. While PSB's are found to be aligned in planes with normal parallel to the direction of the critical resolved shear stress, planar arrays are aligned in the perpendicular direction. Dislocation cell structures, on the other hand, are honycomb configurations in which the walls have

Figure 3: Transmission microscopy picture of Persistent Slip Bands (PSB's) in cyclically-deformed copper. Picture adapted from the work of Essman and Mughrabi [86]

Figure 4: Plannar dislocation arrays. Picture adapted from the work of Neuhauser [61]

high dislocation density, while the cell interiors have low dislocation density. An example of the experimental observations of dislocation cells is shown in Fig. 5, while a schematic illustration of cell evolution from the work of Takeuchi and Argon [67] is illustrated in Fig. 6. cells can be formed under both monotonic [63], [68] and cyclic [58] deformation conditions. However, dislocation cells under cyclic deformation tend to appear after many cycles. Direct experimental observations of these structures have been reported for many materials (e.g. Refs. [1], [68], [63]).

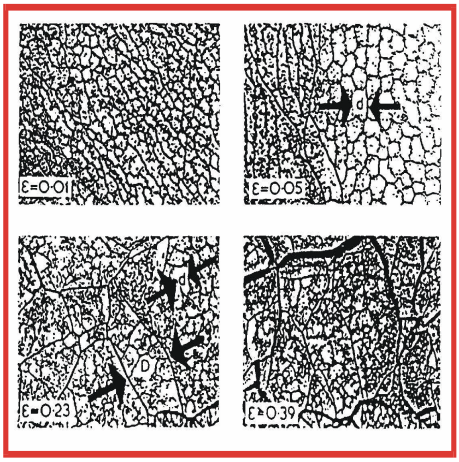

Figure 5: Dislocation cell structure in Iron. Picture adapted from the work of Reppich [68]

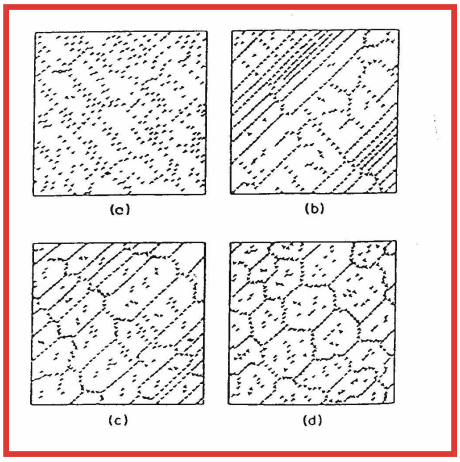

Figure 6: Schematic of Dislocation cell structure evolution. Picture adapted from the work of Takeuchi and Argon [67]

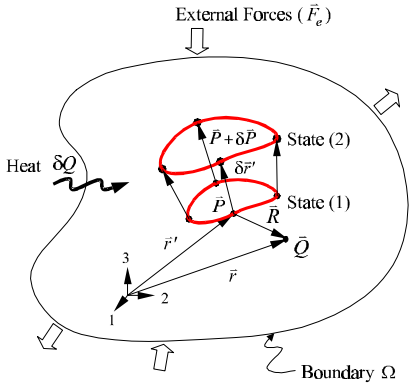

Figure 7: Representation of loop motion in an infinitesimal transition, illustrating thermodynamic variables

3 IRREVERSIBLE THERMODYNAMICS OF DISLOCATION MOTION

Consider a body, volume - and its boundary $\mathcal{S}$, in thermodynamic equilibrium, containing a dislocation loop in an initial position (1), as shown in Fig. 7. Under the influence of external mechanical forces ($\mathbf{F_e}$), and thermodynamic internal forces ($\mathbf{F_i}$), the dislocation loop will undergo a transition from the initial state to a new one designated as (2). Every point on the dislocation loop line is translated to a new position. In the meantime, material points in the body will deform elastically. During this transition of states, energy will be exchanged with the elastic medium, as given by the first law of thermodynamics:

$$dU^t + \delta E^t = \delta Q^t + \delta C^t + \delta W^t \tag{1}$$

where: dU^t is the change in internal energy, δE^t the change in kinetic energy, δQ^t the change in heat energy, δC^t the change in chemical energy by atomic diffusion, and δW^t the change in its mechanical energy. The left hand side of Eq. 1 represents the total change in the energy of the body. We will ignore here changes in the kinetic energy, and restrict the applications of the present model to dislocation speeds less than approximately half of the transverse sound speed (see Refs. [46], [69], [70] for the effects of kinetic energy on the dynamics).

Now the total internal energy can be written as a volume integral: $dU^t = \int dU d\text{-}$, where dU is the specific (per unit volume) change of the internal energy. The mechanical power is composed of two parts: (1) change in the elastic energy stored in the medium upon loop motion under the influence of its own stress. This is precisely the change in the loop self-energy within a time interval δt, (2) the work done on moving the loop as a result of the action of external and internal stresses, excluding the stress contribution of the loop itself . These two components constitute the Peach-Koehler work. Thus: $\delta W^t = \int \sigma_{ik} d\epsilon_{ik} d\text{-}$. Care must be exercised in evaluating the elastic field variables, as will be discussed later. The change in the total chemical energy can be written as a

volume integral of the chemical potential μ_i, over the atomic concentration change dn_i, which is negative for mass transport out of the volume. Additionally, if loop motion produces geometric defects (e.g. jogs and vacancies), chemical energy is deposited. Thus: $\delta C^t = \int \left(dP_d - \sum_i \mu_i dn_i \right) d\text{-}$. Finally, the net change in the heat energy is composed of two parts: (1) heat energy (dH^*) generated by the loop as a result of atomic damping mechanisms (e.g. phonon and electron damping), and (2) heat transported across the boundary to the external reservoir, which is negative by convention. Hence, we have: $\delta Q^t = \int dH^* d\text{-} \; - \int_{\mathcal{S}} \mathbf{Q} \bullet d\mathbf{S}$. Here $\mathbf{Q}$ is the outgoing heat flux at the boundary. Using the divergence theorem for boundary integrals, we obtain:

$$\int \left[(dU - dH^* - dP_d) + (Q_{k,k} + \sum_i \mu_i dn_i - \sigma_{ik} d\epsilon_{ik}) \right] d\text{-} \; = 0 \tag{2}$$

We will denote the enthalpy change $dH = dH^* + dP_d$, as the energy dissipated in defect generation and as heat. It is noted that in the special case where there is no heat or mass transport (i.e. $Q_{i,i} = dn_i = dP_d = 0$), no loop motion (i.e. $\delta W_{PK} = 0$), and under a hydrostatic stress field (i.e. $\sigma_{ik} = -P\delta_{ik}$), we get: $\sigma_{ik} d\epsilon_{ik} = -P\delta_{ik} d\epsilon_{ik} = -P d\epsilon_{ii} = -PdV$, for a unit initial volume. Thus, we recover the familiar relationship between enthalpy and internal energy: $dU = dH - PdV$. For an isothermal process, the Gibbs energy change is given by: $dG = dH - TdS$. Thus:

$$\delta G^t = \int \left[(dU - TdS) + (Q_{i,i} + \sum_i \mu_i dn_i - \sigma_{ik} d\epsilon_{ik}) \right] d\text{-} \tag{3}$$

In addition to energy conservation, loop motion must result in a total increase in the entropy of the body and its surroundings. The Clausius-Duhem statement of the second law of thermodynamics can be phrased as [71]: *"the total entropy production rate of the body and its surroundings must be positive for an irreversible process"*. Following Erringen [71], and Malvern [72], we construct the following entropy production inequality for the solid:

$$\delta \Phi^t = \delta S^t - B - \int_{\mathcal{S}} \mathbf{\Xi} \bullet d\mathbf{S} \geq 0 \tag{4}$$

where $\delta \Phi^t \equiv \int \Phi d\text{-}$ is the total *entropy production* during δt, δS^t the total change in entropy, b the *local entropy source* per unit volume with $B \equiv \int b d\text{-}$, and $\mathbf{\Xi}$ the *entropy influx* due to heat input across the boundary $\mathcal{S}$. Utilizing the divergence theorem again in Eq. 4, we obtain the following inequality per unit volume:

$$\Phi = \delta S - b - \Xi_{k,k} \geq 0 \tag{5}$$

Now, the entropy flux crossing the boundary is: $\mathbf{\Xi} = \frac{\mathbf{Q}}{T}$, and the flux divergence is given by:

$$\Xi_{k,k} = \left(\frac{Q_k}{T} \right)_{,k} = \frac{1}{T} Q_k (lnT))_{,k} - \frac{1}{T} Q_{k,k} \tag{6}$$

While the local entropy source is given by:

$$B = \int \frac{dH}{T} = \int \frac{1}{T} \left[dU + Q_{k,k} - \sigma_{ik} d\epsilon_{ik} + \sum_i \mu_i dn_i \right] d\text{-} \tag{7}$$

Substituting Eqs. 6 and 7 into Eq. 4, we obtain:

$$\int \left\{ (dU - TdS) + Q_k (lnT)_{,k} - \sigma_{ik} d\epsilon_{ik} + \sum_i \mu_i dn_i \right\} d\text{-} \ \leq 0 \tag{8}$$

Comparing the entropy production inequality 8 with Eq. 3, we can immediately see that a consequence of irreversibility (i.e. entropy production) is a *decrease* in Gibbs free energy. Following arguments similar to Erringen [71], we write the internal energy in terms of entropy variations as:

$$\delta G^t = \int \left[(\frac{\partial U}{\partial S} - T)\delta S + Q_k (ln(T))_{,k} - \sigma_{ik} d\epsilon_{ik} + \sum_i \mu_i dn_i \right] d\text{-} \ \leq 0 \tag{9}$$

Since the inequality must be valid for all variations of δS, its coefficient must vanish [71], [72]. Thus, the principle of entropy production results in the following statement:

$$\delta G^t = \int \left[Q_k (lnT)_{,k} - \sigma_{ik} d\epsilon_{ik} + \sum_i \mu_i dn_i \right] d\text{-} \ \leq 0 \tag{10}$$

Under conditions where heat generation during dislocation motion is significant (e.g. high-speed deformation), additional equations must be solved for the coupled point-defect and heat conduction. Thus, equations for point-defect conservation, as well as generalized forms of Fick's and Fourier laws must be added. These are expressed in the following:

$$C^\gamma_{,t} = J^\gamma_{k,k} \tag{11}$$

$$J^\gamma_k = -D^\gamma_{ik} C_{,i} - D_{ik} \left(\frac{Q^* C}{kT^2} \right) T_{,i} \tag{12}$$

$$Q_{\alpha,t} = -\kappa_{ik} T_{,i} - Q^* D_{i\alpha} C_{,i} \tag{13}$$

where $\kappa_{i\alpha}$ is the thermal conductivity tensor, D^γ_{ik} the diffusion tensor of defect γ, Q^* the corresponding heat of transport, and $Q_{k,t}$ the rate of change of the thermal energy.

We treat here the specific case where thermal effects are small (i.e. the first term in Eq. 10 is ignored), and where climb motion of the dislocation loop is a result of point defect absorption (i.e. the third term in Eq. 10 is summed over only vacancies and interstitials). In Eq. 10, the volume integrals of the elastic term and the chemical term (osmotic) can be converted to line integrals over the dislocation loop. The stress tensor acting on any point is decomposed into a contribution resulting from the loop itself (i.e. self- stress $\sigma^{(s)}_{ik}$), and a contribution resulting from other dislocations, defects, Peierls stress, and the applied stress field (i.e. external stress $\sigma^{(e)}_{ik}$). Thus, when the stress tensor in Eq. 10 is written as: $\sigma_{ik} = \sigma^{(s)}_{ik} + \sigma^{(e)}_{ik}$, the elastic term results in two contributions to Gibbs energy, while the chemical term results in one additional contribution. We outline in the following how these three contributions can be converted to line integrals over the loop.

Now consider an infinitesimal variation in the position of a dislocation loop, depicted by the motion of the segments $\bigcup(AB, BC, CD, \cdot\cdot)$ in a time interval δt. During this motion, the dislocation core line length has changed from L to $L + \Delta L$. The dislocation line vector is denoted by $d\mathbf{s} = \mathbf{t} \mid \mathbf{s} \mid$, and the change in position for every atom on the dislocation line is described by the vector $\delta\mathbf{r}$. For the change in the amount of work done on the dislocation loop during its transition from state(1) to state(2) in Fig. 7 above, we assume that the stress field is uniformly acting on every surface element $\mathbf{dA} = \mathbf{b} \times d\mathbf{s}$. The associated element of virtual force is: $d\mathbf{F} = \mathbf{\Sigma} \bullet \mathbf{dA}$. During loop motion from state(1) to state(2), the variation in this Peach-Koehler work [73] obtained by integration along the path Γ is given by:

$$\begin{aligned} \int [\sigma_{ik} d\epsilon_{ik}]^{(e)} d\text{-} \; = \delta W_{PK} &= \oint_{\Gamma} d\mathbf{F} \bullet \delta\mathbf{r} = \oint_{\Gamma} (\mathbf{b} \times d\mathbf{s} \bullet \mathbf{\Sigma}) \bullet \delta\mathbf{r} \\ &= \oint_{\Gamma} (\mathbf{b} \bullet \mathbf{\Sigma} \times \mathbf{t}) \bullet \delta\mathbf{r} \mid d\mathbf{s} \mid \\ &= \oint_{\Gamma} (\in_{ijk} \sigma_{jm} b_m t_k \delta r_i) \mid d\mathbf{s} \mid \end{aligned} \tag{14}$$

The unit vector $\mathbf{t}$ is tangent to the dislocation line, and lies on its glide plane, while $\in_{ijk}$ is the permutation tensor.

The total self- energy of the dislocation loop is obtained by double integrals along the contour Γ. Gavazza and Barnett [74] have shown that the first variation in the self- energy of the loop can be written as a single line integral of the form:

$$\int [\sigma_{ik} d\epsilon_{ik}]^{(s)} d\text{-} \; = \oint_{\Gamma} \left(\left[E(\mathbf{t}) - (E(\mathbf{t}) + E''(\mathbf{t})) \ln(\frac{8}{\varepsilon\kappa}) \right] \kappa - J(L, \mathbf{P}) \right) \mathbf{n} \bullet \delta\mathbf{r} \, |d\mathbf{s}| + [dU]_{core} \tag{15}$$

where $\mathbf{n}$ is normal to the dislocation line vector $\mathbf{t}$ on the glide plane, and $\varepsilon = \mid \mathbf{b}/2 \mid$ is the dislocation core radius [21]. The first term results from loop stretching during the infinitesimal motion, the second and third are the *line tension* contribution, while $J(L, \mathbf{P})$ is a non-local contribution to the self-energy. The dominant contributions to the self-energy (or force) are dictated by the local curvature κ, and contain the pre-logarithmic energy term $E(\mathbf{t})$ for a straight dislocation tangent to the loop at point $\mathbf{P}$, and its second angular derivative E''. $[dU]_{core}$ is the contribution of the dislocation core to the self-energy. Defining the angle between the Burgers vector and the tangent as $\alpha = cos^{-1}(\frac{\mathbf{t} \bullet \mathbf{b}}{|b|})$, Gore [75] showed that a convenient computational form of the self- energy integral for an isotropic elastic medium of $\nu = \frac{1}{3}$ can be written as:

$$\int [\sigma_{ik} d\epsilon_{ik}]^{(s)} d\text{-} \; = \oint_{\Gamma} \left(-\kappa \;\; [E(\alpha) + E''(\alpha)] \ln(\frac{8}{\varepsilon\kappa}) + \mu b^2 [\kappa(\frac{21 + cos^2\alpha}{64\pi}) + \bar{\kappa}(\frac{2 \;\; cos^2\alpha - 1}{2\pi})] \right) \mathbf{n} \bullet \delta\mathbf{r} \, |d\mathbf{s}| \tag{16}$$

where the energy pre-factors are given by:

$$E(\alpha) = \frac{\mu b^2}{4\pi(1-\nu)} (1 - \nu \;\; cos^2\alpha) \tag{17}$$

$$E''(\alpha) = \frac{\mu b^2 \;\; \nu}{2\pi(1-\nu)} cos \;\; 2\alpha \tag{18}$$

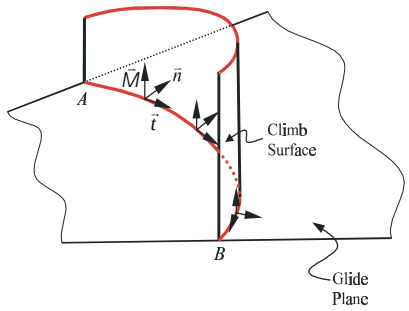

Figure 8: 3-D motion of a curved dislocation segment involving in-plane glide and out-of-plane climb.

Accurate numerical calculations of the self-energy of any complex-shape loop have been performed by Ghoniem and Sun [56], where the double line integral is converted to a fast summation over the loop segments and quadrature points. However, a purely numerical method for evaluation of the self-energy requires intensive computations because of the need to use large quadrature order for good accuracy [56]. Eq. 16 is an alternate convenient approximation, in which the contributions of various terms are easily computed. Schwarz [48] conducted a numerical study to determine the effects of various terms on the self-force, and concluded that the major contribution results from the first two terms in Eq. 16, which are the usual line tension approximation. However, the relative importance of the third term (which represents contributions from the dislocation core and dislocation line stretching) and fourth term (which is an approximation to non-local contributions from other parts of the loop) can be seen by a simple argument. The non-local term is obtained by approximating the loop as a pure shear loop at an average curvature of $\bar{\kappa}$. For a reasonable size loop of approximate radius in the range $1000 - 10000 \mid \mathbf{b} \mid$, it can be shown that the total contribution of non-local, core and stretch terms is on the order of less than 18%. The contribution of the non-local term is about half of this amount for purely edge components. Hence, a computationally efficient and very accurate method is obtained when all contributions are combined in Eq. 16.

Absorption of point defects by dislocation segments can be treated by considering the influence of the chemical term in Eq. 10 on its motion. Incorporation of atomic defects into dislocation cores leads to dislocation climb. The thermodynamic force associated with this motion is referred to as the *osmotic* force. As illustrated in Fig. 8, during climb motion of atoms within the dislocation core, the number of vacancies (or interstitials) per unit length $\frac{dn_\gamma}{L}$, changes by the amount:

$$\frac{dn_\gamma}{L} = \frac{\mid \mathbf{b} \mid \mathbf{m} \bullet \delta \mathbf{r}}{\text{-}_\gamma} \tag{19}$$

where -_γ is the vacancy (interstitial) volume, and $\mathbf{m}$ is a unit vector normal to the glide

plane (see Fig. 8). The change in chemical potential per vacancy (interstitial) is given by:

$$\mu_\gamma = kT \ ln \ (\frac{C_\gamma}{C_\gamma^{eq}}) \tag{20}$$

Here C_γ is the non-equilibrium concentration of vacancies (or interstitials), which may result from quenching, a sudden change in temperature, irradiation or an externally applied stress [78], and C_γ^{eq} is the thermodynamic equilibrium concentration of the atomic defect. The corresponding contribution from point defect flow to the variation in Gibbs energy for the entire loop can now be obtained by line integration. Incorporating Eqs. [14,16,19,20] into inequality 10, we obtain:

$$\delta G^t = -\oint_\Gamma (\mathbf{f}_S + \mathbf{f}_O + \mathbf{f}_{PK}) \bullet \delta\mathbf{r} \mid d\mathbf{s} \mid \leq 0 \tag{21}$$

where we define the following generalized thermodynamic forces:

- $\mathbf{f}_{PK} \equiv$ the *Peach-Koehler force* per unit length $= \mathbf{b} \bullet \mathbf{\Sigma} \times \mathbf{t}$
- $\mathbf{f}_S \equiv$ the *self- force* per unit length

$$\left(-\kappa \ \ [E(\alpha) + E''(\alpha)] \ln(\frac{8}{\varepsilon\kappa}) + \mu b^2[\kappa(\frac{21 + cos^2\alpha}{64\pi}) + \bar{\kappa}(\frac{2 \ cos^2\alpha - 1}{2\pi})]\right)\mathbf{n}$$

- $\mathbf{f}_O \equiv$ the total *Osmotic force* [46] for defect γ per unit length $= -\sum_\gamma \gamma \ \ kT\frac{|\mathbf{b}|}{\gamma} \ ln\left(\frac{C_\gamma}{C_\gamma^{eq}}\right) \ \mathbf{m}$ where $\gamma = (-1)$ for vacancies and$(+1)$ for interstitials

In compact tensor form, Eq. 21 can be written as:

$$\delta G^t = -\oint_\Gamma f_k^t \delta r_k \mid d\mathbf{s} \mid \leq 0 \tag{22}$$

where f_k^t is the k-component of the total force: $\mathbf{f}^t = \mathbf{f}_S + \mathbf{f}_O + \mathbf{f}_{PK}$, and δr_k is the displacement of core atoms in the k-direction.

4 VARIATIONAL FORMULATION FOR THE EQUATIONS OF MOTION

4.1 Governing Integral Equation

Inequality 10 suggests that the components of Gibbs energy can be written as *conjugate* pairs, representing the inner products of *generalized thermodynamic forces* and *generalized displacements*. The equations of motion can thus be obtained if one defines an appropriate set of generalized coordinates and conjugate generalized thermodynamic forces, in such a way as to result in entropy production and a corresponding decrease in δG during a virtual infinitesimal transition. Let's assume that atoms within the dislocation core are transported in some general drift force field, as a consequence of the motion of atomic size defects (e.g. vacancies, interstitials, kinks and jogs). The drift velocity of each atom is

given by Einstein's mobility relationship: $\mathbf{V}_\lambda = \frac{1}{kT}\mathbf{D}\mathbf{f}_\lambda$, where $\mathbf{V}_\lambda$ is the drift velocity, $\mathbf{D}$ is a diffusion tensor, and $\mathbf{f}_\lambda$ is a generalized thermodynamic force representing process λ. Similarly, the flux resulting from a given process can be related to a corresponding thermodynamic force. We consider here three thermodynamic forces: (1) forces of mechanical origin (i.e. *Peach-Koehler forces*), as a result of variations in virtual work on the dislocation loop and variations in the stored elastic energy in the medium when the dislocation changes its shape, (2) gradients in point defect concentrations within the surrounding medium (i.e. *chemical forces*), and finally (3) temperature gradient forces associated with heat flow.

A generalization of the previous analysis can be accomplished if one postulates that near equilibrium, thermodynamic forces are sufficiently *weak* that we might expand the flux in a power series in $\mathbf{f}_\lambda$ [76]. Let's denote $\mathbf{J}_k(\{\mathbf{f}_\lambda\}$ as type-k flux as a result of a generalized thermodynamic force λ, $\{\mathbf{f}_\lambda\}$. Thus, a generalization of Einstein's phenomenological transport relationship is given by:

$$\mathbf{J}_k(\{\mathbf{f}_\lambda\}) = \mathbf{J}_k(0) + \sum_\lambda \left(\frac{\partial \mathbf{J}_k}{\partial \mathbf{f}_\lambda}\right)_0 \mathbf{f}_\lambda + \frac{1}{2}\sum_{\lambda m}\left(\frac{\partial^2 \mathbf{J}_k}{\partial \mathbf{f}_\lambda \partial \mathbf{f}_m}\right)_0 \mathbf{f}_\lambda \mathbf{f}_m + \cdots. \tag{23}$$

In the linear range of irreversible processes, Eq. 23 is restricted to only the first two terms in the expansion. Moreover, at thermodynamic equilibrium in the absence of generalized forces, all modes of atom transport vanish, and the first term, $\mathbf{J}(0)$, is identically zero. Taking the velocity of atoms on the dislocation line (i.e. representing the core) to be proportional to the atomic flux, and defining generalized mobilities via a mobility tensor $\mathbf{L}$ with components: $L_{ij} = \left(\frac{\partial \mathbf{V}_i}{\partial \mathbf{f}_j}\right)_0$, the phenomenological relationship (Eq. 23) is simplified to:

$$\mathbf{V}_\beta(\{\mathbf{f}_\lambda\}) = \sum_\lambda L_{\beta\lambda}\mathbf{f}_\lambda \tag{24}$$

As a consequence of the increase in entropy production Φ, or equivalently the decrease in Gibbs energyδG, Prigogine [76] showed that: $L_{\beta\lambda}\mathbf{f}_\beta\mathbf{f}_\lambda \geq 0$. This relationship gives a positive definite quadratic form, which imposes restrictions on the matrix of coefficients to be positive. The generalized *mobilities* L_{ij} are subject to additional temporal symmetries as a result of the principle of detailed balance, as shown by Onsager [77] : $L_{\beta\lambda} = L_{\lambda\beta}$. The mobility matrix relates the influence of an independent thermodynamic force of the λ-type to the partial flux of the k-type. In most applications of DD so far, the mobility matrix $L_{\lambda\beta}$ is assumed to be diagonal and independent of the type of thermodynamic force. However, we will assume that dislocation mobility is spatially anisotropic, since the speed of screw segments is usually smaller than edge segments as a consequence of the crystal structure. These simplifications lead to direct proportionality between the velocity and total force along each independent direction. Thus, we can denote $B_{\alpha k}$ as a diagonal resistivity (inverse mobility) matrix, and substitute in Eq. 22 to obtain the following equivalent from of the Gibbs energy variation:

$$\delta G^t = -\oint_\Gamma B_{\alpha k} V_\alpha \delta r_k \mid d\mathbf{s} \mid \tag{25}$$

The resistivity matrix can have three independent components (two for glide and one for climb), depending on the crystal structure and temperature. It is expressed as:

$$[B_{\alpha k}] = \begin{bmatrix} B_1 & 0 & 0 \\ 0 & B_2 & 0 \\ 0 & 0 & B_3 \end{bmatrix} \tag{26}$$

Combining Eq. 22 with Eq. 25, we have:

$$\oint_{\Gamma} \left(f_k^t - B_{\alpha k} V_\alpha \right) \delta r_k \mid d\mathbf{s} \mid = 0 \tag{27}$$

The magnitude of the virtual displacement δr_k is not specified, and hence can be arbitrary. This implies that Eq. 27 is actually a force balance equation on every atom of the dislocation core, where the acting force component f_k^t is balanced by viscous dissipation in the crystal via the term $B_{\alpha k} V_k$. However, this is not necessarily desirable, because one needs to reduce the independent degrees of freedom which describe the loop motion, yet still satisfies the laws of irreversible thermodynamics described here. To meet this end, we develop a general method, with greatly reduced degrees of freedom for the motion of dislocation core atoms.

4.2 The Galerkin Method

Assume that the dislocation loop is divided into N_s curved segments, as illustrated in Fig. 1 . The line integral in Eq. 27 can be written as a sum over each parametric segment j, i.e.,

$$\sum_{j=1}^{N_s} \int_j \delta r_i (f_i^t - B_{ik} V_k) \mid d\mathbf{s} \mid = 0 \tag{28}$$

Note that in Eq. 28, we sum over the number of segments j and follow the standard rules of 3-D tensor analysis. We now choose a set of generalized coordinates q_m at the two ends of each segment j. Then, the segment can be parametrically described as:

$$r_i = \sum_{m=1}^{N_{DF}} \mathcal{C}_{im}(u) q_m \tag{29}$$

where $\mathcal{C}_{im}(u)$ are shape functions, dependent on the parameter u ($0 \leq u \leq 1$). Eq. 29 is a general parametric representation of the dislocation line for segment j. Possible convenient parameterization methods are discussed in Refs. [25], [56]. In Sec. 5 we introduce quintic splines as flexible and convenient parametric curves for complex dislocation loop geometry, while the applications in Sec. 7 illustrate the utilization of several types of parametric elements on the same loop. It is noted that the index m is assumed to be summed from 1 to N_{DF}, where N_{DF} is the number of total generalized coordinates at two ends of the loop segment. Accordingly, the three components of displacement vector are given by:

$$\delta r_i = \sum_{m=1}^{N_{DF}} \mathcal{C}_{im}(u) \delta q_m \tag{30}$$

On the other hand, we have for the velocity of any point on the dislocation line, within segment j:

$$V_k = r_{k,t} = \sum_{n=1}^{N_{DF}} \mathcal{C}_{kn} q_{n,t} \tag{31}$$

And the arc length differential for segment j is given by:

$$\mid d\mathbf{s} \mid = (r_{l,u} r_{l,u})^{\frac{1}{2}} du = \left(\sum_{p,s=1}^{N_{DF}} q_p \mathcal{C}_{lp,u} \mathcal{C}_{ls,u} q_s \right)^{\frac{1}{2}} du \tag{32}$$

An ensemble of dislocation loops is considered a continuous dynamical system, where every point on dislocation lines is subject to continuous displacement. The finite element process in continuum mechanics is based on approximating the continuous displacement field by a linear combination of piece-wise known shape functions over specified domains. To obtain the unknown coefficients in the linear combination, an integral form of the governing equation is formulated, and an element-by-element assembly is extracted. The result is a system of equations for *standard discrete systems*, which can be handled by numerical methods. We will follow a similar approach here, in which the weight functions in the integral form are the same as the shape functions of the problem. Minimization of the weighted residuals results in symmetric matrices, which simplifies integration of the equations of motion. This variational approach is thus coincident with the Galerkin method as a special case of the method of weighted residuals. Recently, a number of investigators formulated microstructure evolution problems in a similar manner (see, for example Refs. [79], [80]).

At this point, we may substitute Eqs. 30, 31, and 32 into the governing Eq. 28, and obtain the following form:

$$\sum_{j=1}^{N_s} \int_0^1 \sum_{m=1}^{N_{DF}} \delta q_m \mathcal{C}_{im}(u) \left[f_i^t - B_{ik} \sum_{n=1}^{N_{DF}} \mathcal{C}_{kn} q_{n,t} \right] \left(\sum_{p,s=1}^{N_{DF}} q_p \mathcal{C}_{lp,u} \mathcal{C}_{ls,u} q_s \right)^{\frac{1}{2}} du = 0 \tag{33}$$

Appropriate collection of terms into more convenient functions can reduce the apparent complexity of this form of the equation of motion. We will define here two such functions: an effective force and an effective resistivity. A *generalized force*, f_m, is defined as:

$$f_m = \int_0^1 f_i^t \mathcal{C}_{im}(u) \left(\sum_{p,s=1}^{N_{DF}} q_p N_{lp,u} N_{ls,u} q_s \right)^{\frac{1}{2}} du \tag{34}$$

while a *resistivity matrix* element, γ_{mn}, is given by:

$$\gamma_{mn} = \int_0^1 \mathcal{C}_{im}(u) B_{ik} \mathcal{C}_{kn}(u) \left(\sum_{p,s=1}^{N_{DF}} q_p \mathcal{C}_{lp,u} \mathcal{C}_{ls,u} q_s \right)^{\frac{1}{2}} du \tag{35}$$

It is noted that $[\gamma_{mn}]$ is a symmetric matrix because of the structure of the above definition and symmetric mobilities. With these two parameters defined above, the variational

integral form of the Gibbs energy equation is readily transformed to a discrete form, given by:

$$\sum_{j=1}^{N_s}\left[\sum_{m=1}^{N_{DF}}\delta q_m(f_m-\sum_{n=1}^{N_{DF}}\gamma_{mn}q_{n,t})\right]=0 \tag{36}$$

For the entire dislocation loop, we map all local degrees of freedom $q_i^{(j)}$ of each segment j onto a set of global coordinates, such that the global coordinates are equal to the local coordinates at each beginning node on the segment:

$$\{q_1^{(1)},q_2^{(1)},q_3^{(1)},.....,q_1^{(2)},q_2^{(2)},q_3^{(2)},....\}=\{Q_1,Q_2,Q_3,...,Q_N\}^T \tag{37}$$

where N is the total number of degrees of freedom of the loop. Similar to the finite element procedure, the local segment resistivity matrix $[\gamma_{mn}]$ is added into corresponding global locations in the global resistivity matrix $[\Gamma_{kl}]$, such that:

$$\sum_{j=1}^{N_s}\sum_{m=1}^{N_{DF}}\sum_{n=1}^{N_{DF}}[\delta q_m\gamma_{mn}q_{n,t}]^{(j)}=\sum_{k=1}^{N_{tot}}\sum_{l=1}^{N_{tot}}\delta Q_k\Gamma_{kl}Q_{l,t} \tag{38}$$

where $N_{tot}=N_sN_{DF}$ is the total number of degrees of freedom for the loop. The global resistivity matrix $[\Gamma_{kl}]$ is also symmetric and banded or sparse. The component Γ_{kl} is zero if the degrees of freedom k and l are not connected through a segment. In addition, the global force vector $\{\mathcal{F}_k\}$ can similarly be represented as

$$\sum_{j=1}^{N_s}\sum_{m=1}^{N_{DF}}[\delta q_m f_m]^{(j)}=\sum_{k=1}^{N_{tot}}\delta Q_k\mathcal{F}_k \tag{39}$$

Therefore, Eq. 36 can be expressed as:

$$\sum_{k=1}^{N_{tot}}\delta Q_k\left(\mathcal{F}_k-\sum_{l=1}^{N_{tot}}\Gamma_{kl}Q_{l,t}\right)=0 \tag{40}$$

Since the virtual displacements in the generalized coordinates are totally arbitrary, the previous equation can only be satisfied if:

$$\mathcal{F}_k=\sum_{l=1}^{N_{tot}}\Gamma_{kl}Q_{l,t} \tag{41}$$

Eq. 41 represents a set of time-dependent ordinary differential equations which describe the motion of dislocation loops as an evolutionary dynamical system. Similar microstructure evolution equations have been derived by Suo [80] in connection with grain and void growth phenomena. Furthermore, the above spatially resolved equations can be discretized in time by the so-called *generalized trapezoidal family of methods* [81] as:

$$\sum_{l=1}^{N_{tot}}\Gamma_{kl}^{(n+\alpha)}Q_l^{(n+1)}=\sum_{l=1}^{N_{tot}}\Gamma_{kl}^{(n+\alpha)}Q_l^{(n)}+\Delta t\mathcal{F}_k^{(n+\alpha)} \tag{42}$$

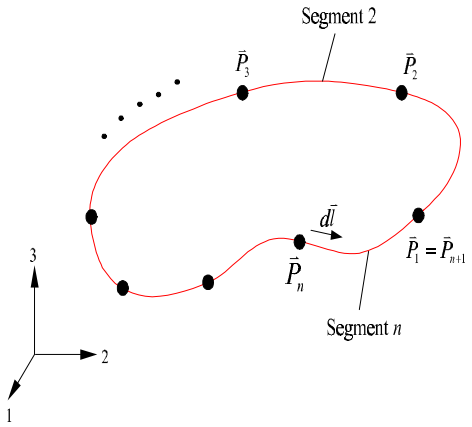

Figure 9: A space dislocation loop discretized into a finite number of curved segments, N_s

where Δt is the time-step and n is the time-step index. In addition, α is a parameter, which determines explicit or implicit time-integration, taken to be in the interval [0,1] such that:

$\alpha = 0$ –for forward difference integration (Euler) ;
$\alpha = 1/2$ – for midpoint or trapezoidal integration;
$\alpha = 2/3$ – for Galerkin integration, and ;
$\alpha = 1$ –for backward difference (Euler) integration.

5 COMPUTATIONAL GEOMETRY OF DISLOCATION LOOPS

The core of an arbitrary-shape, 3-D dislocation loop can be reduced to a continuous line. Assume that the dislocation line is segmented into (n_s) arbitrary curved segments, labeled $(1 \leq i \leq n_s)$, as shown in Fig. 9. For each segment, we define $\hat{\mathbf{r}}(u) = \mathbf{P}(u)$ as the position vector for any point on the segment, $\mathbf{T}(u) = T\mathbf{t}$ as the tangent vector to the dislocation line, and $\mathbf{N}(u) = N\mathbf{n}$ as the normal vector at any point (See Fig. 10). The space curve is then completely described by the parameter u, if one defines certain relationships which determine $\hat{\mathbf{r}}(u)$. Note that the position of any other point in the medium (Q) is denoted by its vector $\mathbf{r}$, and that the vector connecting the source point $\mathbf{P}$ to the field point is $\mathbf{R}$, thus $\mathbf{R} = \mathbf{r} - \hat{\mathbf{r}}$. In the following developments, we restrict the parameter $0 \leq u \leq 1$, although we map it later on the interval $-1 \leq \hat{u} \leq 1$, and $\hat{u} = 2u - 1$ in the numerical quadrature implementation of the method.

To specify a parametric form for $\hat{\mathbf{r}}(u)$, we will now choose a set of generalized coordinates $\mathbf{q}_i^{(j)}$ for each segment (j), which can be quite general. If one defines a set of basis functions $\mathcal{C}_i(u)$, where u is a parameter, and allows for index sums to extend also over the basis set $(i = 1, 2, .., I)$, the equation of the segment can be written as:

$$\hat{\mathbf{r}}^{(j)}(u) = \mathbf{q}_i^{(j)} \mathcal{C}_i(u) \tag{43}$$

Or, in compact component (k) form, this can be put as:

$$\hat{r}_k^{(j)}(u) = q_{ik}^{(j)} \mathcal{C}_i(u) \tag{44}$$

Thus, the components of the displacement vector are given by:

$$\delta\hat{r}_k^{(j)}(u) = \delta q_{ik}^{(j)} \mathcal{C}_i(u) \tag{45}$$

At this point, we must specify the form of parametric description for the dislocation line. Although this step is open to pure computational convenience, we present here those parametric forms which we use later in this work. Parametric dislocation representation discussed below are also sufficient to describe the majority of experimentally observed dislocation line geometry.

5.1 Circular, Elliptic and Helical Loops

Small prismatic loops of circular (or nearly elliptic) shapes are observed in many materials under deformation, irradiation and quenching conditions [82]. Helical loops of unusual regularity have also been experimentally observed under large vacancy supersaturation [82]. Therfore, it seems natural to use a simple representation for such loops, where the shape functions are given by:

$$\mathcal{C}_1 = cos(2\pi u), \qquad \mathcal{C}_2 = sin(2\pi u), \qquad \mathcal{C}_3 = u \tag{46}$$

And their parametric derivatives, which we use later in determining the arc length, are simply given by:

$$\mathcal{C}_{1,u} = -2\pi\mathcal{C}_2, \qquad \mathcal{C}_{1,u} = 2\pi\mathcal{C}_1, \qquad \mathcal{C}_{3,u} = 1 \tag{47}$$

Note that in this case, the description is not in Cartesian coordinates, and that the generalized degrees of freedom are given by:

$$q_1 = a, \qquad q_2 = b, \qquad , and \qquad q_3 = c \tag{48}$$

Loop motion is described in terms of the time variations of the generalized coordinates, a, b, and c.

5.2 Linear Parametric Segments

The majority of 3-D dislocation dynamics developments are based on analytic solutions to the elastic field of linear segments [35]-[49]. Sometimes it is just as convenient to use a purely numerical method, without any loss of computational speed or accuracy [56]. Under these conditions, the *shape functions* $\mathcal{C}_i(u)$ and their derivatives $\mathcal{C}_{i,u}$ take the form:

$$\mathcal{C}_1 = 1 - u \qquad \mathcal{C}_2 = u \qquad and \tag{49}$$

$$\mathcal{C}_{1,u} = -1 \qquad \mathcal{C}_{2,u} = 1 \tag{50}$$

The available degrees of freedom for a *free, or unconnected* linear segment (j) are just the position vectors of the beginning(j) and end $(j+1)$ nodes. Thus:

$$q_{1k}^{(j)} = P_k^{(j)}, \qquad and \qquad q_{2k}^{(j)} = P_k^{(j+1)} \tag{51}$$

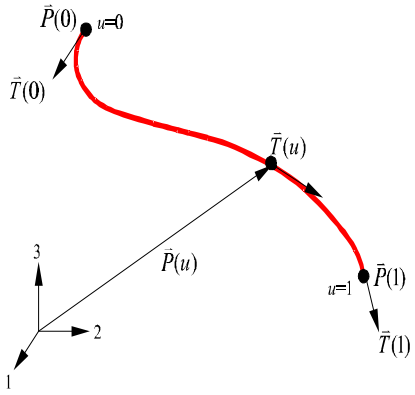

Figure 10: Basic elements of a space curve representing one dislocation segment

5.3 Cubic Spline Parametric Segments

The self-force on a dislocation segment can be approximated as a simple function of its curvature ([15], [16], [74]). To allow for continuity of the self-force along the entire dislocation loop, and to capture non-linear deformations of the dislocation line itself during, a higher order parametric representation is desired. For cubic spline segments, we use the following set of shape functions, their parametric derivatives, and their associated degrees of freedom, respectively:

$$\mathcal{C}_1 = 2u^3 - 3u^2 + 1, \quad \mathcal{C}_2 = -2u^3 + 3u^2, \quad \mathcal{C}_3 = u^3 - 2u^2 + u, \quad and \quad \mathcal{C}_4 = u^3 - u^2 \tag{52}$$

$$\mathcal{C}_{1,u} = 6u^2 - 6u, \quad \mathcal{C}_{2,u} = -6u^2 + 6u2, \quad \mathcal{C}_{3,u} = 3u^2 - 4u + 1, \quad and \quad \mathcal{C}_{4,u} = 3u^2 - 2u \tag{53}$$

$$q_{1k}^{(j)} = P_k^{(j)}, \qquad q_{2k}^{(j)} = P_k^{(j+1)}, \qquad q_{3k}^{(j)} = T_k^{(j)}, \qquad and \quad q_{4k}^{(j)} = T_k^{(j+1)} \tag{54}$$

5.4 Quintic Spline Parametric Segments

A dislocation loop is divided into a set of curved segments connected at their end nodes, with each segment represented as an independent parametric space curve with parameter u varying in the range 0 to 1. A general vector form of the dislocation line equation for segment (j) can be expressed as:

$$\mathbf{r}^{(j)}(u) = \sum_{i=0}^{n} \mathbf{A}_i^{(j)} \; u^i \tag{55}$$

where n is a polynomial order and $\mathbf{A}_i$ represent the associated vector coefficients. The value of n determines the segment type. Thus, when $n = 1$ the segment is a straight line, when $n = 3$ the segment is a cubic polynomial and when $n = 5$, the segment is a fifth-order (quintic) polynomial. The coefficients $\mathbf{A}_i$ are determined by boundary conditions imposed on beginning and end nodes. These boundary conditions can be described in terms of specified geometric properties, such as the nodal position, tangent, curvature, or torsion.

To solve for the six coefficients $\mathbf{A}_0$ to $\mathbf{A}_5$ of a quintic spline segment, we have to assign six independent vectors, to be determined by six boundary conditions $\mathbf{r}^{(j)}(0)$, $\mathbf{r}^{(j)}(1)$, $\mathbf{r}^{(j)}_{,u}(0)$, $\mathbf{r}^{(j)}_{,u}(1)$, $\mathbf{r}^{(j)}_{,uu}(0)$, and $\mathbf{r}^{(j)}_{,uu}(1)$, where $\mathbf{r}^{(j)}_{,u} = d\mathbf{r}^{(j)}/du$ and $\mathbf{r}^{(j)}_{,uu} = d^2\mathbf{r}^{(j)}/du^2$. Geometrically, $\mathbf{r}^{(j)}(0)$ and $\mathbf{r}^{(j)}(1)$ are the position vectors of nodes j and $j+1$, i.e., $\mathbf{P}^{(j)}$ and $\mathbf{P}^{(j+1)}$. The vectors $\mathbf{r}^{(j)}_{,u}(0)$ and $\mathbf{r}^{(j)}_{,u}(1)$ are the tangent vectors of nodes j and $j+1$, i.e., $T^{(j)}_E\mathbf{t}^{(j)}$ and $T^{(j+1)}_B\mathbf{t}^{(j+1)}$, respectively, where $T^{(j)}_E$ and $T^{(j+1)}_B$ are magnitudes of tangent vectors at the end (E) and beginning (B) of each segment, while the unit vectors $\mathbf{t}^{(j)}$ and $\mathbf{t}^{(j+1)}$ are the dislocation sense vectors at nodes j and $j+1$, respectively. The vectors $\mathbf{r}^{(j)}_{,uu}(0)$ and $\mathbf{r}^{(j)}_{,uu}(1)$ are linear combinations of the tangent and normal vectors because they lie on the plane spanned by them. Because the resultant loop profile is a composite curve, dislocation line continuity may not be maintained at each node if boundary conditions on segments are arbitrarily assigned . In general, C^0(position) and C^1(tangent) continuity can be easily satisfied if we assign the same position and tangent vectors at each node. However, since self-forces on dislocation segments are proportional to the local curvature (see Eq. 16, C^2 continuity will ensure the continuity of self-forces at segment nodes as well. The curvature of a general point on segment j can be expressed as

$$\kappa = \frac{\|\mathbf{r}^{(j)}_{,u}(u) \times \mathbf{r}^{(j)}_{,uu}(u)\|}{\|\mathbf{r}^{(j)}_{,u}(u)\|^3} \tag{56}$$

To maintain C^2 continuity at each node, we let the curvature of the end point of segment j be equal to the curvature at the beginning node of curved segment $j+1$.

$$\frac{\|\mathbf{r}^{(j)}_{,u}(1) \times \mathbf{r}^{(j)}_{,uu}(1)\|}{\|\mathbf{r}^{(j)}_{,u}(1)\|^3} = \frac{\|\mathbf{r}^{(j+1)}_{,u}(0) \times \mathbf{r}^{(j+1)}_{,uu}(0)\|}{\|\mathbf{r}^{(j+1)}_{,u}(0)\|^3} \tag{57}$$

From Eq. 57, and the fact that $\mathbf{r}^{(j)}_{,uu}$ is a linear combination of $\mathbf{T}\&\mathbf{N}$, the tangent component of vector $\mathbf{r}^{(j)}_{,uu}$ does not influence the line curvature. Therefore, we can just assign the normal vectors $N^{(j)}_E\mathbf{n}^{(j)}$ and $N^{(j+1)}_B\mathbf{n}^{(j+1)}$ for $\mathbf{r}^{(j)}_{,uu}(1)$ and $\mathbf{r}^{(j+1)}_{,uu}(0)$, respectively, where N^j_E and $N^{(j+1)}_B$ represent magnitudes associated with the unit vectors $\mathbf{n}^{(j)}$ and $\mathbf{n}^{(j+1)}$. After substituting all boundary conditions into Eq. 55 and rearranging terms, we obtain:

$$\mathbf{r}^{(j)}(u) = \mathcal{C}_1\mathbf{P}^{(j)} + \mathcal{C}_2\mathbf{P}^{(j+1)} + \mathcal{C}_3T^{(j)}_E\mathbf{t}^{(j)} + \mathcal{C}_4T^{(j+1)}_B\mathbf{t}^{(j+1)} + \mathcal{C}_5N^{(j)}_E\mathbf{n}^{(j)} + \mathcal{C}_6N^{(j+1)}_B\mathbf{n}^{(j+1)} \tag{58}$$

Note that the superscript on the LHS of Eq. 58 refers to segment j, while on the RHS, it is associated with nodes j and $j+1$ on the same segment. The coefficients $\mathcal{C}_1$ to $\mathcal{C}_6$ are invariant shape functions, and can be expressed in terms of parameter ($0 \le u \le 1$) as:

$$\begin{aligned}
\mathcal{C}_1 &= -6u^5 + 15u^4 - 10u^3 + 1 \\
\mathcal{C}_2 &= 6u^5 - 15u^4 + 10u^3 \\
\mathcal{C}_3 &= -3u^5 + 8u^4 - 6u^3 + u \\
\mathcal{C}_4 &= -3u^5 + 7u^4 - 4u^3 \\
\mathcal{C}_5 &= -0.5u^5 + 1.5u^4 - 1.5u^3 + 0.5u^2 \\
\mathcal{C}_6 &= 0.5u^5 - u^4 + 0.5u^3
\end{aligned}$$

We can cast the parametric Eq. 58 into a convenient matrix form for a single parametric quintic spline of a segment, if we re-organize the generalized coordinates q_m as:

$$\{q_m\} = \{q_1, q_2, q_3, ..., q_{18}\}^T \tag{59}$$

where the first nine components are for the beginning node of the segment; with $q_1 - q_3$ being three components of position, $q_4 - q_6$ three components of the tangent vector, and $q_7 - q_9$ three components of the normal vector. Correspondingly, q_{10} to q_{18} indicate all coordinates at the end of a segment. The shape functions for the quintic spline can also be organized in the following matrix form:

$$[\mathcal{C}_{im}] = \begin{bmatrix} \mathcal{C}_1 & 0 & 0 & \mathcal{C}_3 & 0 & 0 & \mathcal{C}_5 & 0 & 0 & \mathcal{C}_2 & 0 & 0 & \mathcal{C}_4 & 0 & 0 & \mathcal{C}_6 & 0 & 0 \\ 0 & \mathcal{C}_1 & 0 & 0 & \mathcal{C}_3 & 0 & 0 & \mathcal{C}_5 & 0 & 0 & \mathcal{C}_2 & 0 & 0 & \mathcal{C}_4 & 0 & 0 & \mathcal{C}_6 & 0 \\ 0 & 0 & \mathcal{C}_1 & 0 & 0 & \mathcal{C}_3 & 0 & 0 & \mathcal{C}_5 & 0 & 0 & \mathcal{C}_2 & 0 & 0 & \mathcal{C}_4 & 0 & 0 & \mathcal{C}_6 \end{bmatrix} \tag{60}$$

With this notation, Eq. 58 can be cast in the computational form of Eq. 29. The total number of available degrees of freedom for a quintic spline segment is thus equal to the number of components in the Cartesian vector q_m, i.e. $N_{DF} = 6 \times 3 = 18$. However, because of geometric and physical restrictions on dislocation motion, N_{DF} can be greatly reduced, as we will discuss next.

Forces and energies of dislocation segments are given per unit length of the curved dislocation line. Also, line integrals of the elastic field variables are carried over differential line elements. Thus, if we express the Cartesian differential in the parametric form:

$$d\ell_k^{(j)} = \hat{r}_{k,\,u}^{(j)} du = q_{sk}^{(j)}\, \mathcal{C}_{s,\,u} du \tag{61}$$

The arc length differential for segment j is then given by:

$$\mid d\ell^{(j)} \mid \;=\; \left(d\ell_k^{(j)} d\ell_k^{(j)} \right)^{\frac{1}{2}} = \left(\hat{r}_{k,\,u}^{(j)} \hat{r}_{k,\,u}^{(j)} \right)^{\frac{1}{2}} du \tag{62}$$

$$= \left(q_{pk}^{(j)}\, \mathcal{C}_{p,\,u}\;\; q_{sk}^{(j)}\, \mathcal{C}_{s,\,u} \right)^{\frac{1}{2}} du \tag{63}$$

5.5 Constrained Glide Motion and Reduced Degrees of Freedom

It is apparent that general dislocation motion would involve many degrees of freedom N_{DF} in the most general case. Fortunately, however, N_{DF} is small in practice. As a result of segment connectivity at common nodes, only half of the total DF's are required per segment, and $N_{DF} = 9$ for general 3-d motion, and $N_{DF} = 6$ for motion on a glide plane. The Peach-Koehler force on the glide plane imposes an additional constraints. As can be seen from Eqs. 14 and 16 , both external and self-forces on a dislocation node are along the normal direction $\mathbf{n}$. Also, because $\mathbf{n} \bullet \mathbf{t} = 0$, N_{DF} is reduced further from 6 to 4 for 2-d glide motion; that is one for the displacement magnitude, two for the tangent vector, and one for the magnitude of the normal. Furthermore, we introduce here two additional conditions, which simplify the loop profile calculations even further. A *smoothness* condition is invoked such that rapid variations of curvature are avoided when two segments of vastly different lengths are connected via a composite spline. If the magnitude of the tangent is not related to nodal positions, undesirable *cusps* may develop on the dislocation line. Thus, we take the magnitude of the tangent vector to be estimated

from the arc length between previous nodal positions on the segment. This criterion is exact when the parameter $u = s$, where s is the arc length itself. On the other hand, the line curvature can be independently computed from the dislocation configuration and nodal loading in a simple manner. If the forces at the node are not near equilibrium (i.e. the acting forces are much larger than the self-force), the curvature is determined from three neighboring nodes on the dislocation line. On the other hand, near equilibrium, the curvature of a node is readily computed from Eq. 16, once the local external force is known. These approximations can lead to an additional reduction of two degrees of freedom, and we are left with solving for only two equations per node. These constraints can be relaxed, if one is interested in more complex details of dislocation motion. We will show later in Sec. 7 that dislocation glide motion can be adequately described in most cases with only two degree of freedom per node.

We derive here the constrained discrete equations of motion, when dislocation lines are confined to their glide plane. In this special case, there is a total of six independent unknowns. That is, $\Delta P_x, \Delta P_y, \Delta T_x, \Delta T_y, \Delta N_x, \Delta N_y$, which correspond to incremental displacements, tangents, and normals in the x- and y-directions, respectively. Let us first consider the geometric constraints. Because the normal is always perpendicular to the tangent at the node, we have:

$$\begin{aligned} (\mathbf{T}^{(i)} + \Delta\mathbf{T}) \bullet (\mathbf{N}^{(i)} + \Delta\mathbf{N}) &= 0 \\ \Delta T_x \Delta N_x + \Delta T_y \Delta N_y + N_x^{(i)} \Delta T_x + T_x^{(i)} \Delta N_x &+ \\ N_y^{(i)} \Delta T_y + T_x^{(i)} \Delta N_y + T_x^{(i)} N_x^{(i)} + T_y^{(i)} N_y^{(i)} &= 0 \end{aligned} \tag{64}$$

where the symbols with superscript (i) refer to a previous time-step of known values (i.e. $\mathbf{T}^{(i+1)} = \mathbf{T}^{(i)} + \Delta\mathbf{T}$). Furthermore, from a geometric point of view, the curvature of the loop at a current time-step is related to the normal and tangent vectors as:

$$\kappa = \frac{||\mathbf{N}||}{||\mathbf{T}||^2} \tag{65}$$

where the curvature is assumed to be determined by local forces or nodal positions, as discussed earlier. The norm (magnitude) of the current tangent vector is proportional to the previous arc length of a segment. That is:

$$||\mathbf{T}|| = \eta \tag{66}$$

where η is determined by the arc length of the previous time-step. Finally, the displacement vector is perpendicular to the tangent direction of the considered node.

$$\frac{\Delta P_y}{\Delta P_x} = -\frac{T_x^{(i)}}{T_y^{(i)}} = \gamma \tag{67}$$

where γ is a constant determined by previous tangent components. Thus, by introducing an angle θ, which is the angle between the tangent vector and the x-direction, the six independent unknowns can be reduced to only two: ΔP_x and θ, such that all constraints are automatically satisfied:

$$\Delta P_x = \Delta P_x$$

$$
\begin{aligned}
\Delta P_y &= \gamma \Delta P_x \\
\Delta T_x &= \eta cos\theta - T_x^{(i)} \\
\Delta T_y &= \eta sin\theta - T_y^{(i)} \\
\Delta N_x &= -\kappa \eta^2 sin\theta - N_x^{(i)} \\
\Delta N_y &= \kappa \eta^2 cos\theta - N_y^{(i)}
\end{aligned}
$$

Moreover, a linearization technique can be used to approximate sine and cosine functions in terms of $\Delta\theta$, as long as the time-step is small, and hence the tangent angle variation is small between time-steps. Based on the above constraints, Eq. **??** may finally be simplified with a reduced set of shape functions $\tilde{\mathcal{C}}$ as:

$$
\{\delta r_i\} = \left[\tilde{\mathcal{C}}_{im}(u)\right] \{\delta q_m\} \tag{68}
$$

where:

$$
\{\delta r_i\} = \begin{Bmatrix} \delta x \\ \delta y \end{Bmatrix} \tag{69}
$$

$$
\{\delta q_m\} = \begin{Bmatrix} \delta P_{xB} \\ \delta \theta_B \\ \delta P_{yE} \\ \delta \theta_E \end{Bmatrix} \tag{70}
$$

$$
\left[\tilde{\mathcal{C}}_{im}(u)\right] = \begin{bmatrix} \mathcal{C}_1 & \mathcal{D}_1 & \mathcal{C}_2 & \mathcal{D}_2 \\ \gamma\mathcal{C}_1 & \mathcal{D}_3 & \gamma\mathcal{C}_2 & \mathcal{D}_4 \end{bmatrix} \tag{71}
$$

and

$$
\begin{aligned}
\mathcal{D}_1 &= -\eta_L \mathcal{C}_3 sin\theta_B - \kappa_B \eta_B^2 \mathcal{C}_5 cos\theta_B \\
\mathcal{D}_2 &= -\eta_E \mathcal{C}_4 sin\theta_E - \kappa_E \eta_E^2 \mathcal{C}_6 cos\theta_E \\
\mathcal{D}_3 &= \eta_L \mathcal{C}_3 cos\theta_B - \kappa_B \eta_B^2 \mathcal{C}_5 sin\theta_B \\
\mathcal{D}_4 &= \eta_E \mathcal{C}_4 cos\theta_E - \kappa_E \eta_E^2 \mathcal{C}_6 sin\theta_E
\end{aligned}
$$

It is noted that the subscripts B and E refer to *Beginning* and *End* nodes of one segment of the dislocation loop.

5.6 Adaptive Protocols for Node and Time-step Assignments

Because of the evolving nature of dislocation line geometry as a result of strong interactions, it is highly desirable to develop adaptive methods which capture essential physics without excessive computations. Control of the magnitude of the computational time-step, and nodal positions on each segment has a direct influence on the final accuracy of DD simulations. For node redistribution, we first compute a reference curvature $\bar{\kappa}$ for the entire loop, which is normally taken as the average curvature of all nodes. Then, we compare the curvature κ_i of each node with $\bar{\kappa}$, and classify nodes into high curvature groups ($\kappa_i > \bar{\kappa}$) and low curvature groups ($\kappa_i < \bar{\kappa}$). Finally, we increase the number of nodes for each high curvature group and decrease the number of nodes for each low curvature group. After adding or removing nodes, we redistribute the nodes evenly for that group.

To prevent the number of nodes from increasing or decreasing too fast, we only add or remove one node at a time. If the number of nodes for a low curvature group is less than a specified minimum, we keep the current nodes because a prescribed minimum number of nodes is required to maintain the loop geometry. After redistributing nodes on each segment, we calculate the displacement and tangent angle of each new node based on the current loop geometry. The radius of curvature of each new node is determined by a linear interpolation from old nodes for open loops, or by circular arc approximations for closed loops. The highest curvature occurs always at fixed nodes or in the close proximity of other dislocations. In regions of high curvature, large self-forces occur and the curvature at the segment will be near its equilibrium value. Thus, the curvature in these special locations can be determined directly from the equilibrium condition on the segment. The entire geometry of the loop is finally determined by using Eq. 58 at next time-step.

Time-step selection is determined by dislocation segment velocity and its adjacency to other segments. The time-step is selected such that, on average, dislocation-dislocation interaction is resolved within about 100 steps. If the dislocation density is ρ, the average distance between segments is on the order of $\rho^{-1/2} \sim 10^{-5} - 10^{-6}$ m. In fcc crystals, the dislocation resistivity is on the order of 5×10^{-5} Pa s, while it is about 8 orders of magnitude higher for screw segments in bcc crystals [83]. These considerations lead to a time-step of $\sim 1ns$ for fcc crystals and $\sim 0.1s$ for bcc crystals at low temperatures. When two loop segments approach each other, a short-range reaction occurs, and the time-step must be reduced to determine whether the reaction will lead to annihilation or junction formation. In case of annihilation, two loops join together and form different new loops as a mode of plastic recovery. On the other hand, junction formation leads to hardening and stabilization of dislocation patterns. In either case, the minimum distance between segments on the loop itself, or on two adjacent loops is determined by calculating all local minimum distances from each node to a curved segment. By scanning all possible nodes of on a loop, we obtain the minimum distance d_{min} between two loops or between two segments on the loop itself. If this value is less than two times the maximum displacement, i.e. $2d_{max}$, then the time-step is adjusted to $0.25d_{min}/d_{max}$. This procedure is repeated until loop annihilation or junction formation is completed. After annihilation or junction formation is completed, the time-step is gradually increased to its maximum assigned value, as discussed above. During short-range encounters, local dislocation segment velocity can approach the sound speed, and inertial effects may have to be accounted for, if one is interested in the exact details of the short-range reaction (see [70]).

If new loops are generated during the short-range reaction, all nodes on the loop are rearranged. For loop junction formation, new loops are not generated, and the nodes are ordered to allow formation of straight junction segments. However, five possible cases for generating new loops are considered during segment annihilation. On the glide plane, a full dislocation loop may be totally closed, or may have closure on other glide plane via sessile threading arms. Thus, we may have one of the following possibilities:(1) annihilation of two segments on the same open loop to produce one new open loop and one new closed loop; (2) annihilation of two segments on the same closed loop to produce two new closed loops; (3) annihilation of two segments on two different open-loops to produce two new open loops; (4) annihilation of two segments, one an open loop and the other on a closed one to produce one new open loop; (5) annihilation of two segments on two different closed loops to produce one new closed loop. In each case, the nodes on generated loops

are reordered.

6 ELASTIC FIELD VARIABLES AS FAST SUMS

In this section, we present a reasonably self-consistent discussion of isotropic elastic theory which leads to the present fast sum computational implementation. A number of equivalent formulations are available in the literature [16], [15], [84]. However, because the present development is mainly computational, we follow the tensor index formulation of deWit [21], Kröner [18], and Kroupa [20]. The following discussion outlines the basic notation and main relationships in elastcity theory, which will be used throughout this section and associated appendices.

The position vector dyadic is written as: $\mathbf{r} = r_i \mathbf{e}_i$, where $(r_i = x, y, z)$,and $(\mathbf{e}_i)$ are three unit vectors along the Cartesian directions for $(i = 1, 2, 3)$. The magnitude of the position vector is: $r = (r_i r_i)^{\frac{1}{2}}$, while the displacement vector is: $\mathbf{u} = u_i \mathbf{e}_i$. The components of the deformation gradient tensor are: $u_{i,j} = \frac{\partial u_i}{\partial r_j}$, while the components of the symmetric strain tensor are given by: $\epsilon_{ij} = \frac{1}{2}(u_{i,j} + u_{j,i})$. The equations of translational and rotational equilibrium, and the stress-strain relations, respectively, are given by:

$$\sigma_{ij,j} + f_i = C_{ijkl} u_{k,lj} + f_i = 0 \tag{72}$$

$$\sigma_{ij} = \sigma_{ji} \tag{73}$$

$$\sigma_{ij} = C_{ijkl} \epsilon_{kl} = C_{ijkl} u_{k,l} \tag{74}$$

Where (C_{ijkl}) is a fourth rank tensor of 81 components. Because the strain energy density $W = \frac{1}{2}\sigma_{ij}\epsilon_{ij} = \frac{1}{2} C_{ijkl}\epsilon_{ij}\epsilon_{kl}$ is single valued, then: $C_{ijkl} = C_{klij}$. Now, let $I \equiv ij$, and $J \equiv kl$, and utilize the following engineering notation:

$$\sigma_1 \equiv \sigma_{11}, \quad \sigma_2 \equiv \sigma_{22}, \quad \sigma_3 \equiv \sigma_{33}, \quad \sigma_4 \equiv \sigma_{23}, \quad \sigma_5 \equiv \sigma_{13}, \quad \sigma_6 \equiv \sigma_{12} \tag{75}$$

$$\epsilon_1 \equiv \epsilon_{11}, \quad \epsilon_2 \equiv \epsilon_{22}, \quad \epsilon_3 \equiv \epsilon_{33}, \quad \epsilon_4 \equiv 2\epsilon_{23}, \quad \epsilon_5 \equiv 2\epsilon_{13}, \quad \epsilon_6 \equiv 2\epsilon_{12} \tag{76}$$

Then, the stress-strain relationship can be expressed as: $\sigma_I = C_{IJ}\epsilon_J$, where $I, J = 1, 2, 3, ..., 6$. For an isotropic elastic solid, the number of independent elastic constants are only two, given by the following relations:

$$C_{11} = C_{22} = C_{33} = \lambda + 2\mu \tag{77}$$

$$C_{44} = C_{55} = C_{66} = \mu \tag{78}$$

$$C_{12} = C_{13} = C_{23} = \lambda \tag{79}$$

Where $\lambda = G$ and μ are Lamé's constants. The general stress-strain equation may finally be put in the form:

$$\sigma_{ij} = 2\mu\epsilon_{ij} + \lambda\delta_{ij}\epsilon_{kk} \tag{80}$$

It is also easy to show that, for an isotropic material, the elastic constants can be cast in the form:

$$C_{ijkl} = \mu(\delta_{ik}\delta_{jl} + \delta_{il}\delta_{jk}) + \lambda\delta_{ij}\delta_{kl} \tag{81}$$

6.1 The Displacement Field

The displacement field associated with a dislocation loop is given in its computational form in this section. We follow the development of deWit [21], [54], and provide sufficient detail to allow for future elaborations. Derivation steps are given in Appendices B & C.

The dislocation is formed by cutting over an arbitrary surface S, followed by *rigid* translation of the negative side of (S^-), while holding the positive side (S^+) fixed, as illustrated in Fig. 11. Define the dislocation line vector, **t** , as the tangent to the dislocation line. The Burgers vector **b** is prescribed as the displacement jump condition across the surface (S). The elastic field is based on Burgers equation [85], which defines the distribution of elastic displacements around dislocation loops. The strain tensor can be obtained from deformation gradients, while the stress tensor is readily accessible through linear constitutive relations. Once the stress and strain tensors are found, elastic self and interaction energies can be obtained. Referring to Fig. 11, we define the dislocation loop by cutting over the surface S, translating the negative side by the vector **b**, while holding the positive side fixed. Along any *linking curve* Γ, the closed line integral of the displacement vector is **b**. Thus:

$$\mathbf{b} = \oint_{\Gamma} d\mathbf{u} \quad , or b_i = \oint_{\Gamma} u_{i,j} dx_j \tag{82}$$

For a given force distribution $f_m(\hat{\mathbf{r}})$ in the medium, the displacement vector is given by:

$$u_k(\mathbf{r}) = \int_{allspace} U_{km}(\mathbf{r} - \hat{\mathbf{r}}) f_m(\hat{\mathbf{r}}) d^3\hat{\mathbf{r}} \tag{83}$$

Where $U_{km}(\mathbf{r} - \hat{\mathbf{r}})$ are the isotropic elastic Green's functions, given by:

$$U_{km}(\mathbf{R}) = \frac{1}{8\pi\mu}\left[\delta_{km} R_{,pp} - \frac{\lambda+\mu}{\lambda+2\mu} R_{,km}\right]$$

For the volume $\hat{V}$, bounded by the surface $\hat{S}$, and upon utilization of the divergence theorem, we obtain (see Appendix B):

$$u_m(\mathbf{r}) = -b_i \int_{\hat{S}} C_{ijkl} U_{km,l}(\mathbf{r} - \hat{\mathbf{r}}) dS_j \tag{84}$$

For an elastic isotropic medium, the fourth rank elastic constants tensor is given in terms of Lamé's constants. Substituting Eq. 81 into Eq. 84, and re-arranging terms, the displacement vector is given by:

$$\begin{aligned} u_m(\mathbf{r}) &= \frac{1}{8\pi}\int_{\hat{S}} b_m R_{,ppj} d\hat{S}_j \\ &+ \frac{1}{8\pi}\int_{\hat{S}} (b_l R_{,ppl} d\hat{S}_m - b_j R_{,ppm} d\hat{S}_j) \\ &+ \frac{1}{4\pi}\left(\frac{\lambda+\mu}{\lambda+2\mu}\right)\int_{\hat{S}} (b_j R_{,ppm} d\hat{S}_j - b_k R_{,kmj} d\hat{S}_j) \end{aligned} \tag{85}$$

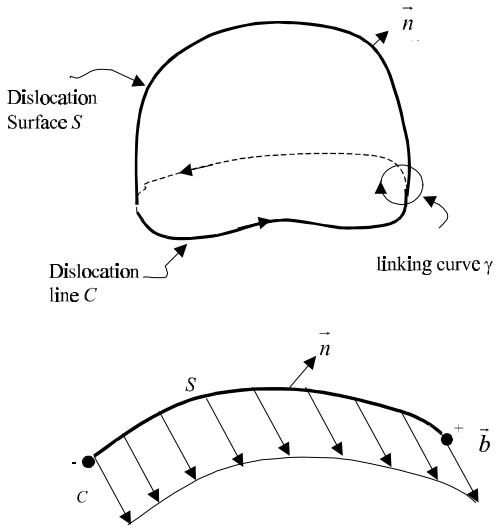

Figure 11: Creation of a dislocation by a cut on the surface (S)

Eq. 85 can be converted to a line integral, if one recalls Stokes Theorem, extended to any rank tensor T, expressed as: $\int\limits_S \in_{ijk} T_{abc\cdots,i} dS_k = \oint\limits_C T_{abc\cdots} dl_j$. Noting the relationship between the Kronecker and permutation tensors, i.e. $\in_{ijk}\in_{klm} = \delta_{il}\delta_{jm} - \delta_{im}\delta_{jl}$, allows us to write Stokes theorem as: $\int\limits_S (\delta_{il}\delta_{jm} - \delta_{im}\delta_{jl})\, T_{abc\cdots,j} dS_i = \oint\limits_C \in_{lmj} T_{abc\cdots} dl_j$. Using the substitution property of the Kronecker delta, Stokes' theorem can also be expressed in the *hat* coordinates in the following form:

$$\int\limits_{\hat{S}} \left(T_{abc\cdots,m} d\hat{S}_l - T_{abc\cdots,l} d\hat{S}_m \right) = \oint\limits_C \in_{klm} T_{abc\cdots} dl_k \tag{86}$$

The first integral in Eq. 85 is the solid angle fraction subtended by the loop times the burgers vector (see Appendix A), while utilization of Eq. 86 can reduce the second and third terms to their line integral form. Therefore, a convenient form for the displacement vector components is given by:

$$u_i = -\frac{b_i}{4\pi} + \frac{1}{8\pi} \oint\limits_C \left[\in_{ikl} b_l R_{,pp} + \frac{1}{1-\nu} \in_{kmn} b_n R_{,mi} \right] dl_k \tag{87}$$

Eq. 87 determines the displacement field of a single dislocation loop. For a loop ensemble, one can use the property of linear superposition. Thus, the line integral in Eq. 87 can be converted into a fast numerical sum over the following set: quadrature points ($1 \leq \alpha \leq Q_{max}$) associated with weighting factors (w_α), loop segments ($1 \leq \beta \leq N_s$), and number of ensemble loops ($1 \leq \gamma \leq N_{loop}$). Therefore, a computational form for the displacement vector is:

$$u_i = \frac{1}{4\pi} \sum_{\gamma=1}^{N_{loop}} \left\{ -b_i + \frac{1}{2} \sum_{\beta=1}^{N_s} \sum_{\alpha=1}^{Q_{max}} w_\alpha \left(\in_{ikl} b_l R_{,pp} + \frac{\in_{kmn} b_n R_{,mij}}{1-\nu} \right) \hat{r}_{k,u} \right\} \tag{88}$$

In appendix A, we list successive derivatives for the modulus of the radius vector $\mathbf{R}$, surface and line integral forms of the solid angle - , and its derivatives. Detailed derivation steps in the equation sequence can be reviewed in Ref. [57].

6.2 Strain and Stress Fields

Once the displacement field is determined, the strain and stress fields can be readily obtained. If we denote the deformation gradient tensor by u_{ij}, the strain tensor e_{ij} in infinitesimal elasticity is its symmetric decomposition: $u_{ij} = \frac{1}{2}(u_{i,j} + u_{j,i}) + \frac{1}{2}(u_{i,j} - u_{j,i}) = e_{ij} + \omega_{ij}$, where ω_{ij} is the rotation tensor. Taking the derivatives of Eq. 85 yields the deformation gradient tensor:

$$u_{i,j} = -\frac{b_j\text{- }_{,i}}{4\pi} + \frac{1}{8\pi}\oint_C \left[\in_{jkl} b_l R_{,ppi} + \frac{1}{1-\nu} \in_{kmn} b_n R_{,mij}\right] dl_k \tag{89}$$

From which the following strain tensor is obtained:

$$e_{ij} = -\frac{b_i\text{- }_{,j} + b_j\text{- }_{,i}}{8\pi} + \frac{1}{8\pi}\oint_C \left[\frac{1}{2}\left(\in_{jkl} b_l R_{,i} + \in_{ikl} b_l R_{,j}\right)_{,pp} + \frac{\in_{kmn} b_n R_{,mij}}{1-\nu}\right] dl_k \tag{90}$$

The derivatives of the solid angle - are given by Eq. 112 in Appendix A, which can now be used to derive the strain tensor components as line integrals.

$$e_{ij} = \frac{1}{8\pi}\oint_C \left[-\frac{1}{2}\left(\in_{jkl} b_i R_{,l} + \in_{ikl} b_j R_{,l} - \in_{ikl} b_l R_{,j} - \in_{jkl} b_l R_{,i}\right)_{,pp} + \frac{\in_{kmn} b_n R_{,mij}}{1-\nu}\right] dl_k \tag{91}$$

Similar to Eq. 88, the fast sum equivalent of Eq. 91 is now given by:

$$e_{ij} = \frac{1}{8\pi}\sum_{\gamma=1}^{N_{loop}}\sum_{\beta=1}^{N_s}\sum_{\alpha=1}^{Q_{max}} w_\alpha \left(-\frac{1}{2}\left(\in_{jkl} b_i R_{,l} + \in_{ikl} b_j R_{,l} - \in_{ikl} b_l R_{,j} - \in_{jkl} b_l R_{,i}\right)_{,pp} + \frac{\in_{kmn} b_n R_{,mij}}{1-\nu}\right) \hat{r}_{k,u} \tag{92}$$

To deduce the stress tensor, we use the isotropic stress-strain relations of linear elasticity. First, the dilatation is obtained by letting both $i\&j = r$ in Eq. 91 above: $e_{rr} = -\frac{1}{8\pi}\frac{1-2\nu}{1-\nu}\oint_C \in_{kmn} b_n R_{,mrr} dl_k$. Using the stress-strain relations: $\sigma_{ij} = 2\mu e_{ij} + \lambda e_{rr}\delta_{ij}$, we can readily obtain the stress tensor.

$$\sigma_{ij} = \frac{\mu b_n}{4\pi}\oint_C \left[\frac{1}{2} R_{,mpp}\left(\in_{jmn} dl_i + \in_{imn} dl_j\right) + \frac{1}{1-\nu} \in_{kmn} \left(R_{,ijm} - \delta_{ij} R_{,ppm}\right) dl_k\right] \tag{93}$$

The *computational* fast sum for the stress tensor is given below in compact form, while explicit representation are listed in appendix D.

$$\sigma_{ij} = \frac{\mu}{4\pi}\sum_{\gamma=1}^{N_{loop}}\sum_{\beta=1}^{N_s}\sum_{\alpha=1}^{Q_{max}} b_n w_\alpha \left[\frac{1}{2} R_{,mpp}\left(\in_{jmn} \hat{r}_{i,u} + \in_{imn} \hat{r}_{j,u}\right) + \frac{1}{1-\nu} \in_{kmn} \left(R_{,ijm} - \delta_{ij} R_{,ppm}\right) \hat{r}_{k,u}\right] \tag{94}$$

6.3 Interaction and Self Energies

The mutual interaction between two dislocation loops can be obtained by a volume integration of the energy density resulting from the stress field of one loop, acting on the strain field of the other, as given below.

$$E_I = \int_V \sigma_{ij}^{(1)} e_{ij}^{(2)} dV \tag{95}$$

where $\sigma_{ij}^{(1)}$ is the elastic stress field from the first dislocation loop and $e_{ij}^{(2)}$ is the elastic strain tensor originating from the second one. After a lengthy derivation, deWit [21] provided a simple double line integral formulation for the interaction energy as:

$$E_I = -\frac{\mu b_i^{(1)} b_j^{(2)}}{8\pi} \oint_{C^{(1)}} \oint_{C^{(2)}} \left[R_{,kk} \left(dl_j^{(2)} dl_i^{(1)} + \frac{2\nu}{1-\nu} dl_i^{(2)} dl_j^{(1)} \right) + \frac{2}{1-\nu} \left(R_{,ij} - \delta_{ij} R_{,ll} \right) dl_k^{(2)} dl_k^{(1)} \right] \tag{96}$$

In Eq.(96), the line integral is carried over the two space curves $C^{(1)}\&C^{(2)}$. Thus, the corresponding fast sum for the interaction energy reads:

$$E_I = -\frac{\mu b_i^{(1)} b_j^{(2)}}{8\pi} \sum_{\beta^{(1)}=1}^{N_s^{(1)}} \sum_{\beta^{(2)}=1}^{N_s^{(2)}} \sum_{\alpha^{(1)}=1}^{Q_{max}^{(1)}} \sum_{\alpha^{(2)}=1}^{Q_{max}^{(2)}} w_{\alpha^{(1)}} w_{\alpha^{(2)}} \times$$
$$\left[R_{,kk} \left(\hat{r}_{j,u}^{(2)} \hat{r}_{i,u}^{(1)} + \frac{2\nu}{1-\nu} \hat{r}_{i,u}^{(2)} \hat{r}_{j,u}^{(1)} \right) + \frac{2}{1-\nu} \left(R_{,ij} - \delta_{ij} R_{,ll} \right) \hat{r}_{k,u}^{(2)} \hat{r}_{k,u}^{(1)} \right] \tag{97}$$

The self-energy of a single dislocation loop can be calculated as $\frac{1}{2}$ the interaction energy between two identical dislocation loops separated by a distance r_0. The contribution to the self energy from the dislocation core can be estimated from atomistic calculations, and is usually on the order of 5-10% of the self energy [20]. However, the core contribution can be incorporated by adjusting the value of r_0. In a fairly rough evaluation, we may take the core energy into account by setting $r_0 = \frac{b}{2}$. (cf. [21])

7 APPLICATIONS OF THE FAST SUM METHOD

In this section, we discuss several test cases which both illustrate the utility of the fast sum method, and validate its accuracy. We will first present results of computations for the elastic field of isolated circular shear and prismatic dislocation loops. Since some analytical solutions are available for these cases, we will compare the results of the fast sum method to analytical results. The issues of numerical convergence and accuracy are also discussed. In the latter part of this section, we present results of calculations of the elastic field of typical complex-shape loops, representing familiar Frank-Read dislocation sources in crystalline materials.

7.1 Stress Field of Simple Loops

1. Circular Slip Loop

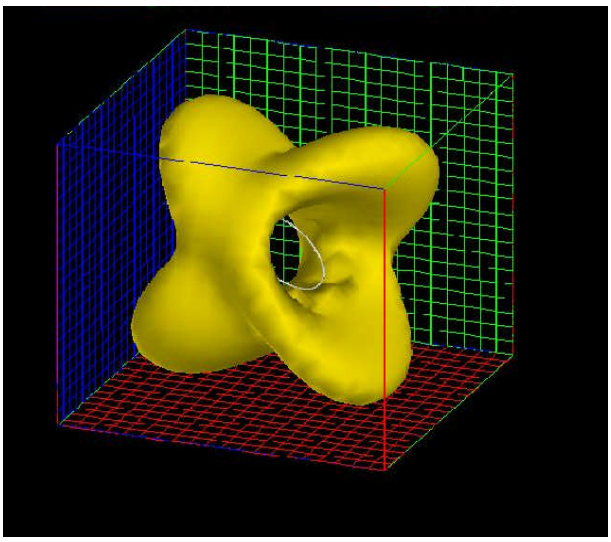

Figure 12: Normal stress iso-surface, σ_{11}, in the local loop coordinates, where the 1-axis is [010]-direction and the 3-axis is the [110]-direction.

We consider here the stress distribution in the vicinity of a shear (slip) loop in a BCC crystal. The circular loop has a radius of 200 $|\mathbf{b}|$. The loop is oriented for primary slip (i.e. $(110)/\frac{1}{2}\{111\}$). In the figures shown in this section, all distances are given in units of $|\mathbf{b}|$,while stress values are relative to μ. In the local coordinates of the (110)-plane, Fig. (12) shows an iso surface for the normal stress around the dislocation loop. It is clear that the stress surface has an orientational dependence on the $< 111 >$-slip direction. On the glide plane itself, the normal stress vanishes, while the stress surface is symmetric with respect to the loop center. The shear stress components σ_{12} and σ_{23} are displayed in FIGS. 5 and 6. While σ_{12} shows a characteristic "lope" structure of the iso-surface, σ_{23} displays a crescent shape, where the maximum width is for pure edge, while the stress vanishes for the screw component of the loop.

The convergence and computational speed of the fast sum method is demonstrated in reference [56]. The dependence of the numerical results on the number of segments, segment spline type, and quadrature indicate that the method is numerically convergent, as the number of segments and/or quadrature integration points is increased [56]. The issue of numerical accuracy of the method is addressed next, by comparison to one of the few available analytical solutions in the literature.

2. Circular Prismatic Loop

Kroupa [20] derived analytical solution for the stress field of a prismatic circular dislocation loop in an infinite isotropic medium. His explicit out-of-plane normal stress in the loop plane (i.e., $z = 0$) σ_z reads:

$$\frac{\sigma_z}{\frac{\mu b}{2\pi R(1-\nu)}} = \frac{2}{1-(\frac{x}{R})^2} E(\frac{x}{R}) \qquad (0 \leq \frac{x}{R} < 1), \qquad (98)$$

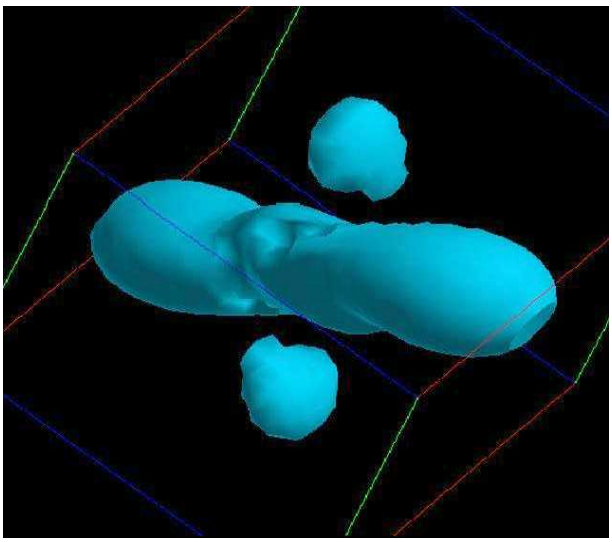

Figure 13: Shear stress iso-surface, σ_{12}, in the local loop coordinates, where the 1-axis is [010]-direction and the 3-axis is the [110]-direction.

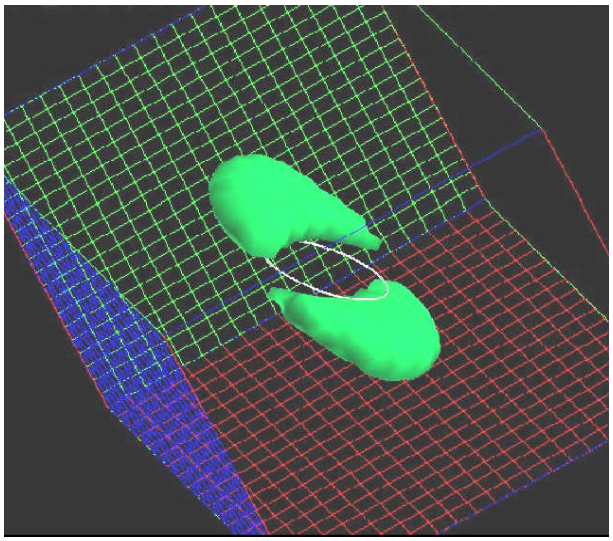

Figure 14: Shear stress iso-surface , σ_{23}, in the local loop coordinates, where the 1-axis is [010]-direction and the 3-axis is the [110]-direction.

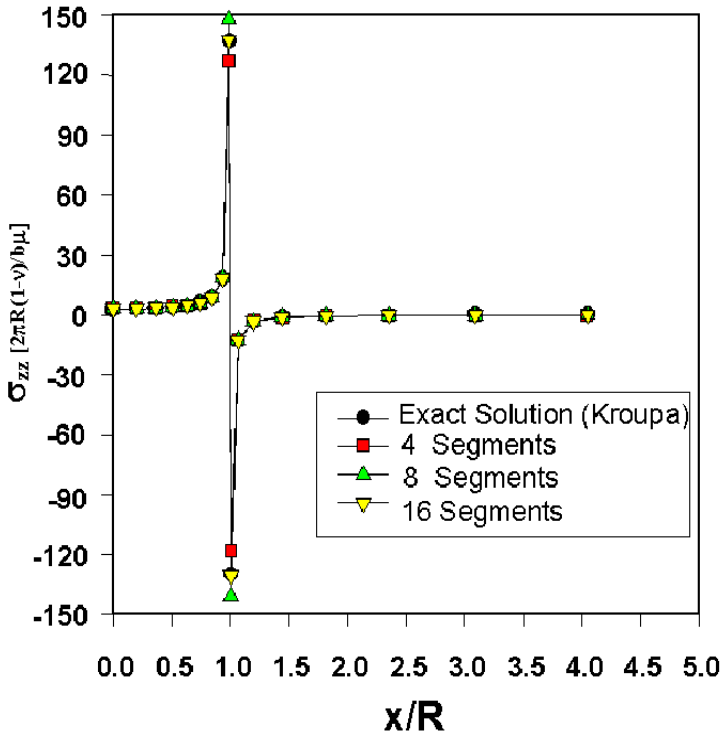

Figure 15: A comparison between numerical (current method) and exact analytical (Kroupa) solutions for the normal stress component σ_{zz} of a circular prismatic loop.

$$\frac{\sigma_z}{\frac{\mu b}{2\pi R(1-\nu)}} = 2\frac{R}{x}\left[K(\frac{R}{x}) - \frac{1}{1-(\frac{R}{x})^2}E(\frac{R}{x})\right] \qquad (\frac{x}{R} > 1) \tag{99}$$

where K and E are the complete elliptic integrals of the first and second kind, respectively, x is the distance from loop center, and R the loop radius.

In order to evaluate the accuracy of the present fast sum method, a comparison between Kroupa's analytical solution for the normal stress component, σ_{zz}, of a circular prismatic loop and our numerical calculations is shown in Fig. 7. It can be seen that the error in the value of the normal stress depends on the number of segments and on the distance between the field point and the dislocation core. The normal stress shows the characteristic asymmetric singularity at the dislocation line, where the stress field decays to zero at large distances from the core, while it remains finite at the loop center. A more quantitative measure of the error is shown in Fig. 8, where the percent error between the numerical and analytical solutions is shown as a function of distance along the x-axis on the loop plane. It is seen that the numerical accuracy is below 4% for only four cubic spline segments, except very close to the dislocation core. The number of quadrature integration points is kept at 16 for all cases studied in the figure. The highest error (below 9%) is manifest at distances less than 1.5 $|\mathbf{b}|$ from the dislocation core, when the number of segments is less than 8. However, the maximum error is less than 0.3% at such close distances, when the number of segments is increased to 16. It is important to note that such

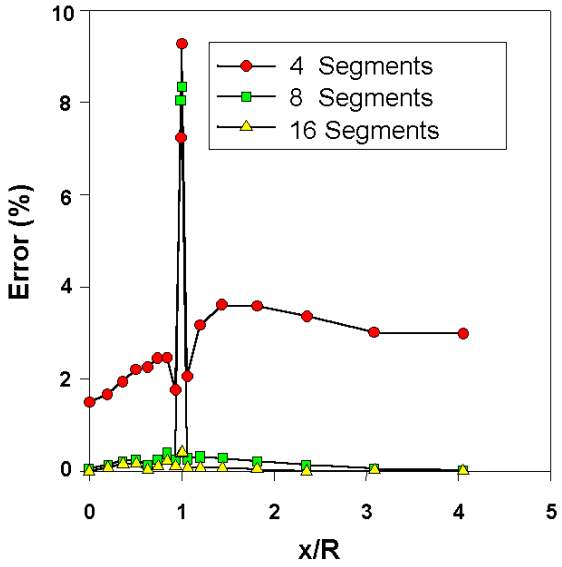

Figure 16: Dependence of the error between numerical and analytical (Kroupa) normal stress results on the distance from loop center, for various number of segments.

high accuracy is needed in calculations of the self-force via the Brown formula [52], or its variants [74], [48]. When the stress field is averaged at distances of $\pm\epsilon$ from the dislocation core, the singularity is removed and a convergent, finite self-force is obtained. Thus, the accuracy of field evaluation is apparent.

7.2 Interaction and Self Energies

To demonstrate the capability of our fast sum calculation of the interaction energy(E_I), we specify the two dislocations to be pure prismatic coaxial circular loops of equal radius and of the same Burgers vector. In such case, the exact analytical result is available from [21] as:

$$\frac{E_I}{2\pi R\mu b^2} = \frac{\kappa}{2\pi(1-\nu)}(K(\kappa) - E(\kappa)) \tag{100}$$

in which $\kappa = \left[\frac{1}{1+(d/2R)^2}\right]^{1/2}$ and d is the normal distance between the two parallel loop planes. Fig. 9 shows the results of our calculations, as compared with exact analytical results. The interaction energy is shown as a function of distance between the two loop planes. While the number of quadrature integration points in these calculations is kept at 128, the interaction energy is convergent as the number of segments is increased. This is particularly important at close distances, as can be seen from the figure.

Furthermore, Hirth and Lothe [16] provided an explicit expression for the self-energy of a circular slip loop as:

$$\frac{E_s}{2\pi R\mu b^2} = \frac{2-\nu}{8\pi(1-\nu)}\left[-ln\left(tan\frac{\rho}{4R}\right) - 2cos\frac{\rho}{2R}\right] \tag{101}$$

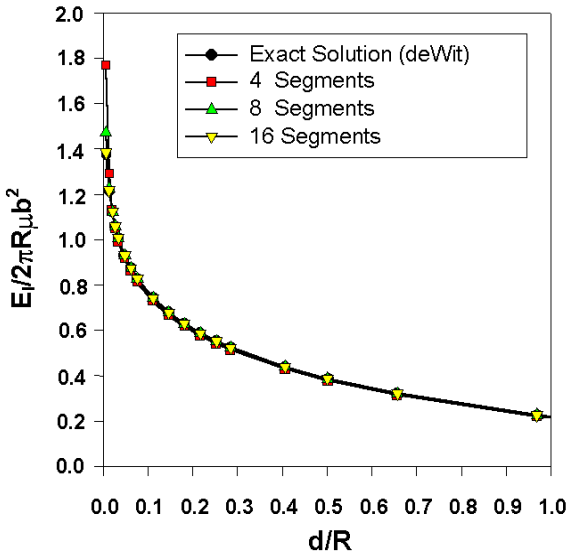

Figure 17: A comparison between numerical (current method) and analytical (deWit) results for the interaction energy between two prismatic loops.

where ρ is the dislocation core size and is taken as $\frac{1}{2|\mathbf{b}|}$, as suggested by deWit [21]. Fig. 10 shows the dependence of the self-energy on the loop radius, computed numerically, and compared to the analytical solutions [16]. The percent error between the numerical and analytical results is shown in Fig. 11. It is interesting to note that, even for four cubic spline segments, the error is rather small (a few percent), when the loop radius is in the tens-to-hundreds of $|\mathbf{b}|$. However, it is clearly demonstrated that more spline segments is necessary for larger size loops, and that the error can generally be brought down below 1%.

7.3 Complex Loop Geometries

1. Single Frank-Read Source

   In typical Dislocation Dynamics computer simulations, heavy initial dislocation microstructure is introduced, and its subsequent evolution is followed by solving appropriate equations of motion. Visualization of the stress field associated with the evolving microstructure requires additional techniques to mask specific features, otherwise the 3-D computer image is hopelessly complicated to be useful. Nonetheless, it is instructive to investigate the nature of the elastic field resulting from reasonably complex loop configurations. In this section, we present results for two common dislocation problems: an isolated Frank-Read (FR) dislocation loop, and two interacting such sources in a Molybdenum single crystal. An initial straight edge dislocation segment, lying on the $(1\bar{1}1)$-plane is subjected to an applied stress. The pinned ends of the segment are located at $x = \pm 100|\mathbf{b}|$ from the plane center of the crystal. The expansion of the dislocation segment results in the dislocation loop, shown in Fig. 12, before annihilation of the two opposite screw components takes place. The

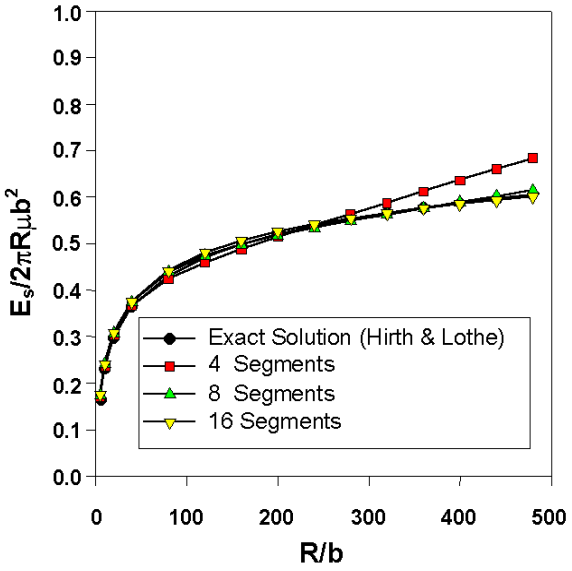

Figure 18: A comparison between numerical (current method) and analytical (Hirth and Lothe) results for the self energy of a slip loop.

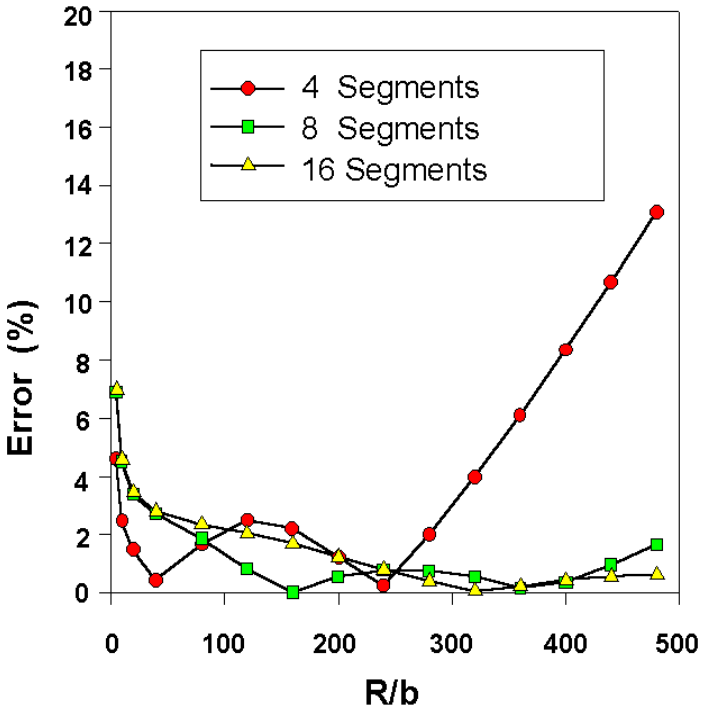

Figure 19: Dependence of the error between numerical and analytical solutions in Fig. 18 above on the loop radius and number of cubic spline segments.

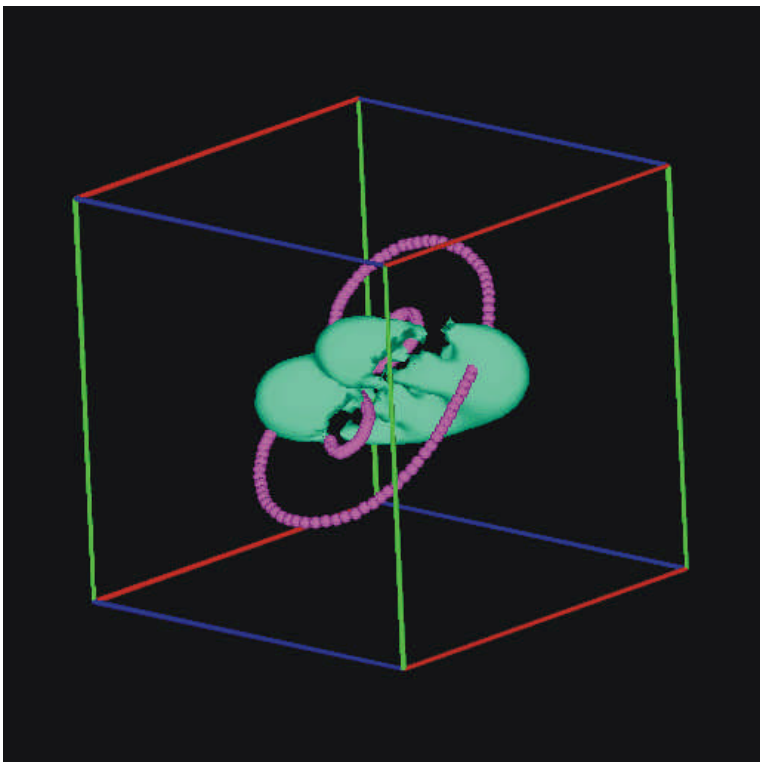

Figure 20: Normal stress iso-surface (186 MPa), σ_{11}, for a single Frank-Read source in Molybdenum

pinned ends of the source are connected to the crystal surface by two rigid threading dislocations. Fig. 12 shows the normal stress iso-surface of (186 MPa)associated with the FR loop. The iso-surface shows orientational dependence on the Burgers vector, as well as symmetry with respect to the (111)-plane. Note the "dimples" in the stress surface which result from the deviation of the FR loop from perfect circular symmetry, as investigated in the earlier section.

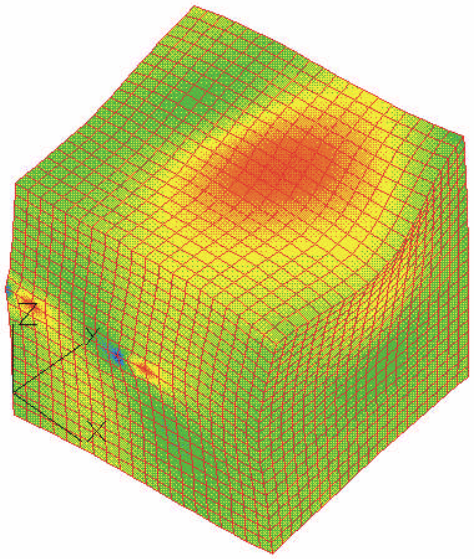

Figure 21: Normal stress distribution resulting from the interaction of the single FR source with the surface of a Molybdenum single crystal

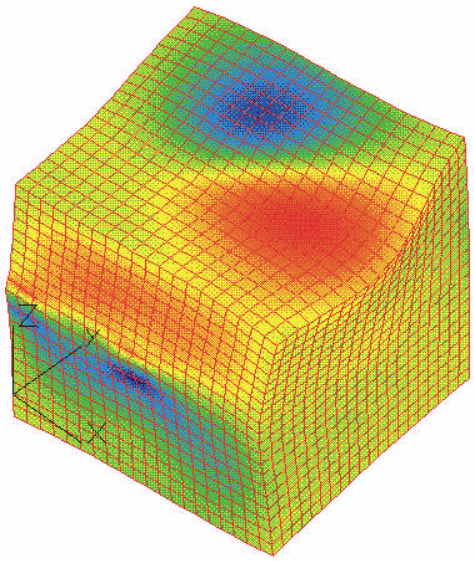

Figure 22: Shear stress distribution resulting from the interaction of a single FR source with the surface of a Molybdenum single crystal

2. Interacting FR Dislocation Loops

So far, we have assumed that the crystal is elastically isotropic and of infinite dimensions. The solution method relies on the existence of analytic forms for the elastic Greens functions, and those are not available for finite media. Recently, Cleveringa, Needleman and Van der Giessen [33] have proposed a superposition method to satisfy the boundary conditions of crystals under external constraints. First, the surface traction resulting from the interaction of the dislocation loop with the crystal surface are computed. Once this is achieved, a Finite Element Method (FEM) is used to calculate the stress field resulting from the same traction, with a reversed sign (so-called image traction, in addition to other externally applied forces. The case of a free crystal is somewhat special, because only image traction boundary conditions can be imposed at the surface. Thus, and since a full dislocation loop is mechanically balanced, only rigid body displacements need to be carefully eliminated. We choose here to use the threading dislocation arms, which intersect the surface at two points, to eliminate rigid body rotation and translation. To show the effects of crystal boundaries, we follow the FEM approach, as suggested by Cleveringa et al. [33]. Fig. 13 shows the results of FEM calculations for the normal stress component on the crystal surface, resulting from image traction. It is clear that the FR source is pulling on the upper surface, and that additional stress concentrations on the $x-z$ surface are associated with the rigid arms of the threading dislocation. The image shear stress σ_{13} is also shown in Fig. 14, where the surface displacements of the crystal are scaled to show the shape of a free crystal which contains an FR source. Note the symmetry with respect to the (111)-plane of positive and negative shear, and the high shear stress around the end points of the threading dislocation.

When FR sources are activated on the same or neighboring slip planes, very complex patterns can emerge [48]. Interaction of FR sources appears to be one of the main mechanisms which control complex dislocation patterns. For this reason, we study the stress field of two such FR sources, which are both located on the $(1\bar{1}1)$-plane. The length of each initial straight edge segment is taken as $150|\mathbf{b}|$. one pinned end of the first FR source is located at $x = 225|\mathbf{b}|$, and at $x = -225|\mathbf{b}|$ for the second source. The other end is located by rotating the initial segment (i.e. $length = 150|\mathbf{b}|$ with an angle of $\theta = 220^o$, and $\theta = 100^o$ for the first and second FR source, respectively.

The normal stress $\sigma_{33} = -130$ MPa is shown in Fig. 15, while the shear stress iso-surface $\sigma_{13} = 170$ MPa is shown in Fig. 16. The normal stress iso-surface shows a split about the (111)-plane, but because of the initial lack of symmetry of the dislocation loop lines, the stress surface is likewise un symmetric. However, Fig. 16 shows an interesting mirror-like symmetry of the stress iso-surface and the original geometry of the FR-sources. This observation is only seen at high levels of stress, where there is nearly no overlap between the stress fields of various segments of the dislocation microstructure. In any event, going beyond the configurations presented here would introduce additional complexities, which are best utilized in computations of Peach-Kohler forces on dislocation segments.

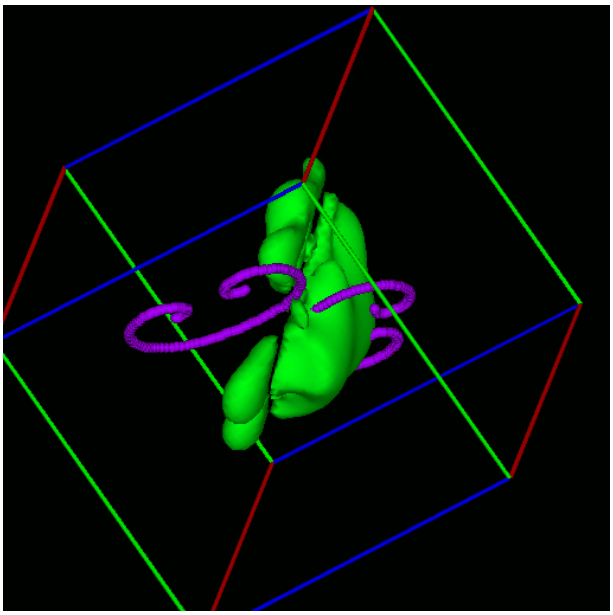

Figure 23: Normal stress iso-surface(-130 MPa), σ_{33}, for two interacting Frank-Read sources in Molybdenum

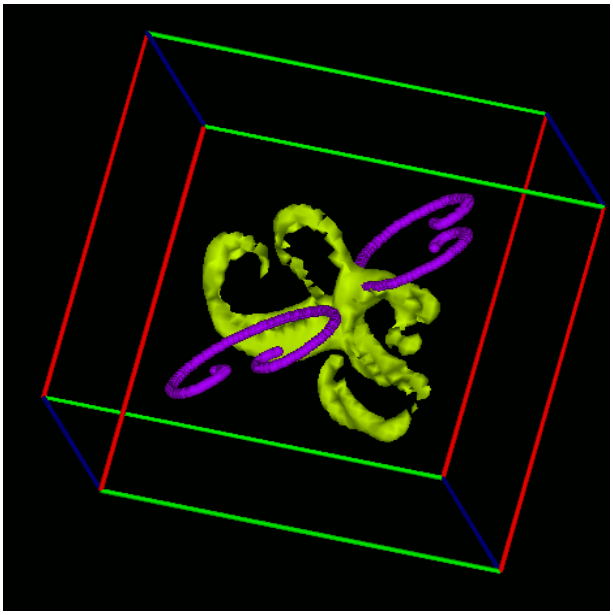

Figure 24: Shear stress iso-surface(170 MPa), σ_{13}, for two interacting Frank-Read sources in Molybdenum

8 COMPUTER SIMULATION OF PLASTIC DEFORMATION

8.1 Illustrative Example: Initial Bow-out of a Pinned Dislocation

To illustrate the computational procedure involved in the present method, we consider here a very simple example, where the equations of motion can be solved analytically for one time-step. Our purpose here is to highlight the essential features of the present computational method. More complex examples, which require extensive computations will be given in the next section. Assume that we are interested in determining the shape of a dislocation line, pinned at two ends and under the influence of pure shear loading on its glide plane. The glide mobility is assumed to be isotropic and constant, and the segments will be taken as linear for illustrative purposes only. The dislocation line is pinned at points L and R, with only two linear and equal segments connected at point A, as shown in Fig. 25. We will compute the shape of the line, advancing it from its initial straight configuration to a curved position. Under these simplifications, the variation in Gibbs free energy, δG for any one of the two segments is given by:

$$\delta G = -B \int_0^1 V \delta r \mid d\mathbf{s} \mid = - \int_0^1 f^t \delta r \mid d\mathbf{s} \mid \tag{102}$$

Now, we expand the virtual displacement and velocity in only two shape functions: $\mathcal{C}_1 = u, \quad \mathcal{C}_2 = 1 - u$. Thus:

$$\delta r_k = \delta q_{ik} \mathcal{C}_i \tag{103}$$

$$V_k = q_{ik,t} \mathcal{C}_i \tag{104}$$

Since we allow the displacement to be only in a direction normal to the dislocation line (y-direction), we drop the subscript k as well. For arbitrary variations of δq_{ik}, the following equation is applicable to any of the two segments (LA, AR).

$$- \int_0^1 \Delta t \times (f_{PK} + f_S) \mathcal{C}_i \mid ds \mid = -B \int_0^1 \Delta q_m \mathcal{C}_m \mathcal{C}_i \mid ds \mid \tag{105}$$

Eq. 105 can be explicitly integrated over a short time interval Δt. The *resistivity matrix* elements are defined by: $\gamma_{im} \equiv B \int_0^1 \mathcal{C}_i \mathcal{C}_m \mid \mathbf{ds} \mid$, and the *force vector* elements by: $f_i \equiv \int_0^1 \mathcal{C}_i \times (f_{PK} + f_S) \mid \mathbf{ds} \mid$. With these definitions, we have the following (2×2) algebraic system for each of the two elements:

$$\Delta q_m \gamma_{im} = f_i \times \Delta t \tag{106}$$

For any one linear element, the line equation can be determined by:

$$\begin{bmatrix} x \\ y \end{bmatrix} = \begin{bmatrix} u & 0 \\ 0 & (1-u) \end{bmatrix} \begin{Bmatrix} q_1 \\ \\ q_2 \end{Bmatrix} \tag{107}$$

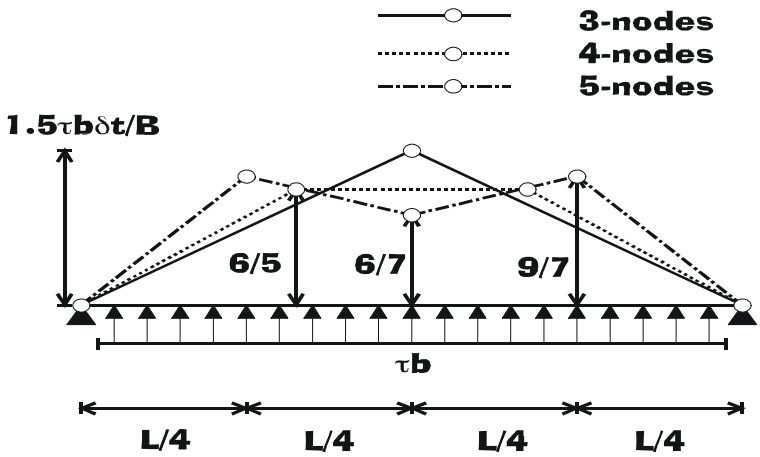

Figure 25: Nodal displacements for the first time-step of an initially straight segment.

And the resistivity matrix can the be simplified as:

$$[\gamma_{mn}] = \frac{Bl}{6}\begin{bmatrix} 2 & 1 \\ 1 & 2 \end{bmatrix} \tag{108}$$

Furthermore, as a result of the shear stress τ and the absence of self-forces during the first time-step only, the distributed applied force vector reads:

$$\{f_m\} = \frac{\tau bl}{2}\begin{Bmatrix} 1 \\ \\ 1 \end{Bmatrix} \tag{109}$$

Since the dislocation line is divided into two equal segments, we can now assemble the force vector, stiffness matrix and displacement vector in the global coordinates, and arrive at following equation for the global nodal displacements ΔQ_i:

$$\frac{Bl}{12}\begin{bmatrix} 2 & 1 & 0 \\ 1 & 4 & 1 \\ 0 & 1 & 2 \end{bmatrix}\begin{Bmatrix} \Delta Q_1 \\ \Delta Q_2 \\ \Delta Q_3 \end{Bmatrix} = \frac{\tau bl\Delta t}{4}\begin{Bmatrix} 1 \\ 2 \\ 1 \end{Bmatrix} + \Delta t\begin{Bmatrix} F_1 \\ 0 \\ F_3 \end{Bmatrix} \tag{110}$$

An important point to note here is that at the two fixed ends, we know the boundary conditions, but the reaction forces needed to satisfy overall equilibrium are unknown. These reactions act on the fixed obstacles at $L\&R$, and are important in determining the overall stability of the configuration (e.g. if they exceed a critical value, the obstacle is destroyed, and the line is released). If $\Delta Q_1 = \Delta Q_3 = 0$ at both fixed ends, we can easily solve for the nodal displacement $\Delta Q_2 = \frac{3}{2}\frac{\tau b\Delta t}{B}$ and for the unknown reaction forces at the two ends: $F_1 = F_3 = -\frac{1}{8}\tau bl$. If we divide the dislocation line into more equal segments, the size of the matrix equation expands, but nodal displacements and reaction forces can be calculated similarly. Results of analytical solutions for successively larger number of nodes on the dislocation segment are shown in Fig. 25.

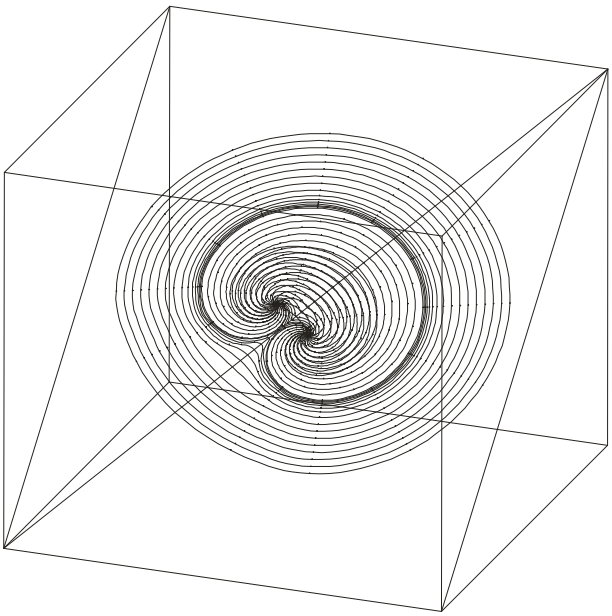

Figure 26: Operation of the Frank-Read source for isotropic dislocation mobility on the glide plane.

8.2 Dislocation Loop Generation

Generation of new dislocation loops is an important process in determining the rate of hardening in materials under deformation. The basic mechanism involves the propagation of a dislocation segment from two immobile (fixed) ends under the action of applied stress. If the applied stress exceeds the resistance offered by the self-force, lattice friction, and additional forces from nearby dislocations, the segment length will increase. In fcc metals, the Peierls (friction) stress is very small, on the order of $10^{-5}\mu$, and is thus lower than typical applied stresses of $10^{-3}\mu$. Dislocation mobility is isotropic at all relevant temperatures because of the low value of Peierls stress in comparison to applied and self stresses on dislocation segments. Thus, the influence of the underlying crystal structure on dislocation generation is not pronounced. On the other hand, high anisotropic Peierls stresses in both fcc and diamond cubic (dc) materials (e.g. Si) imposes constraints on the shapes of generated dislocation loops in these systems, as discussed next.

8.2.1 Isotropic Mobility of Screw and Edge Segments

Fig. 26 shows the results of shape computations for the Frank-Read source in a bcc crystal at high temperature, where the dislocation segment mobility can be assumed to be isotropic on the $< 110 >$ glide plane. In this simulation, we use composite quintic spline segments to construct the loop after each time-step computation of the nodal displacement and tangent angle. The loop starts from an edge line segment with two fixed ends normal to the $< 11\bar{1} >$-direction, for which we assign only three nodes at the first time-step. The tangent vectors at the two end nodes are those of circular arcs constructed from three adjacent nodes. When the loop expands, more nodes are added around the two fixed end nodes (high curvature regions), while the number of nodes is automatically reduced in the

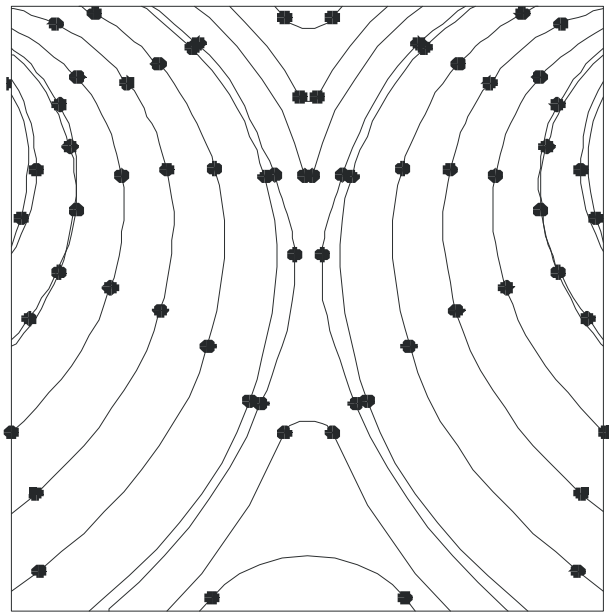

Figure 27: Details of nodal arrangements before annihilation of opposite-character segments.

low curvature region of the loop. After each time-step, the minimum distance between loop segments is calculated. If the minimum distance is detected to be less than $6|\mathbf{b}|$, and $cos^{-1}(\mathbf{t}_1 \bullet \mathbf{t}_2) = (1. \pm 0.05)\pi$, the two segments are annihilated. Here, $\mathbf{t}_1$&$\mathbf{t}_2$ are the tangent vectors for segments 1 and 2, respectively. The value of $6|\mathbf{b}|$ for the critical annihilation distance in fcc is taken from experimental measurements on Cu [86] and Ni [87]. Results of calculations are shown in Fig. 26, where nodal positions are indicated on each loop. Details of node rearrangement before and after an annihilation reaction between two curved segments on the Frank-Read source are shown in Fig. 27. The influence of the self-force on dislocation motion is significant, especially during short-range interaction of dislocation segments. In Fig.28, the angular distribution of the self-force on the glide dislocation loop, immediately after its formation by annihilation of opposite segments on the original dislocation line is shown. It is clear that the distribution of the self-force is negative everywhere on the loop, except for the small range of angles surrounding the newly formed dislocation segment. In this region, the self-force is positive, and thus it will assist the applied stress in expanding this curved region faster than others on subsequent time-steps. The action of applied and self-forces tend to even out curvature variations on the entire loop, once the short-range reaction is completed. The self-force is seen to be higher for the screw segments at $\theta = 90^o$&270^o, as compared to segments with a pure edge character.

Fig. 29 illustrates the operation of a single Frank-Read source on the $< 111 >$-plane in an fcc metal, where discrete barriers to dislocation motion are successively overcome by the expanding loop. The computational protocol detects the existence of random barriers, such as other dislocations piercing the plane or defect clusters, and the loop is divided into two segments anchored at each barrier as a new node. The barrier strength is determined by a critical angle between the tangent to the dislocation and the normal to the node

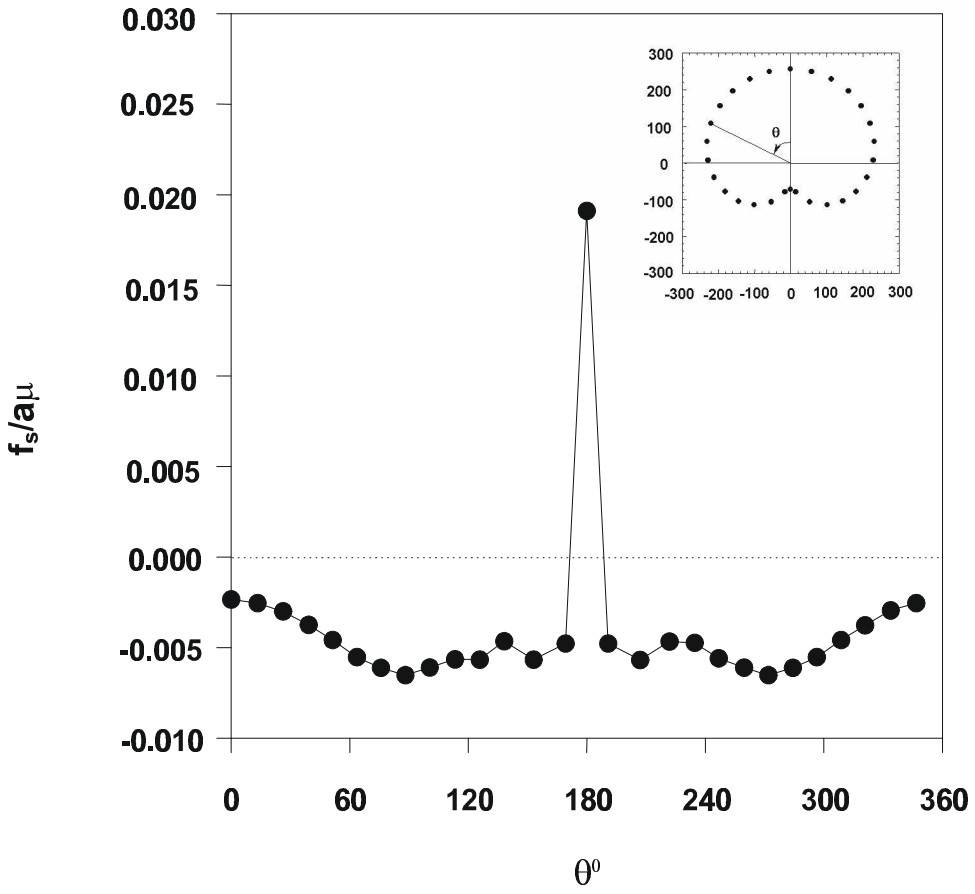

Figure 28: Angular variation of the self force (units of $\frac{\sigma}{\mu a}$) in copper for the Frank-Read source after segment annihilation. The angle θ is defined in the insert. All distances on the figure are in units of the lattice constant.

at the bottom of the barrier. This critical angle has been determined to be $\sim 70^o$ for dislocation intersections in Cu by MD simulations [88].

8.2.2 BCC metals at low temperature

In bcc metals, the primary slip system is $\{110\} < 111 >$, although slip on secondary $\{112\}\&\{123\}$ planes are possible [46]. Slip trace analysis at low temperature [89], [90] indicates that the main slip planes are $\{110\}$, and that dislocations are either of the screw or edge type. At temperatures below $T_a \sim 0.15T_m$, dislocations in bcc metals tend to move as straight lines, indicating that the mobility of the edge component is extremely high [83]. The mobility of screw segments is controlled by double kink nucleation below the *athermal* temperature, T_a. Peierls lattice friction stress on screw components is very high, and the corresponding mobility is low. As the temperature increases, the influence of lattice friction on screw component mobility is reduced, and the mobility of screw and edge dislocations become comparable. It is expected, therefore, that dislocations become very straight at low temperatures, and that significant curvatures develop at higher temperatures. To adequately represent this physical picture, we use composite cubic spline curves joined with linear segments when necessary, and still maintain C^2 continuity at all nodes. In this case, the tangent directions of each curved segment are pre-determined by crystallography (i.e. $< 111 >$-directions for screw components), and only the magnitude of the tangent vector needs to be calculated from the condition of continuity. Additionally, nodes on expanding loops in this case are not re-distributed, but are selected to ensure construction of polygonal loop shapes, as is experimentally observed at low-temperature [90]. The construction procedure of polygonal loop geometry is described as follows.

First, straight linear segments are assigned parallel to specific crystallographic directions (i.e. $< 111 >$) for screw components. The displacement is computed for the entire linear segment in the normal edge direction. Then, two adjacent nodes at each corner of a the resulting rectangle are assigned, such that the distance of each node from the corner is proportional to the magnitude of the displacement, which is determined by the anisotropic mobility. Finally, after nodes are generated, the tangent direction of each node is aligned with the side of the polygon or is assigned a prescribed angle with the polygonal direction as an additional degree of freedom. For example, if the temperature is increased in bcc crystals, slight curvatures can be expected, and the tangent magnitudes can be solved for by applying the condition of C^2 continuity (Eq. 57). It is noted that at very low-temperatures in bcc metals, the mobility of edge components (kinks) is much higher than that of screw segments, and thus dislocation lines will be predominantly of the screw type. These features of adaptive shape computations are illustrated in Fig. 30 for low-temperature and Fig. 31 for higher temperatures.

8.2.3 Dislocation Sources in Si

Motion of dislocations on the glide plane of dc crystals, such as Si, occurs by breaking and re-construction of strong covalent bonds. Thus, the resistance of the lattice to dislocation motion is significant up to very high temperatures (e.g 1200 K in Si). The dislocation must overcome a large energy barrier in the direction of maximum bond strength (i.e. the three $< 110 >$ close-packed directions on the $\{111\}$-family of slip planes), and a smaller one in directions $\pm 60^o$ to those primary ones. Dislocation segment mobility in Si is rather

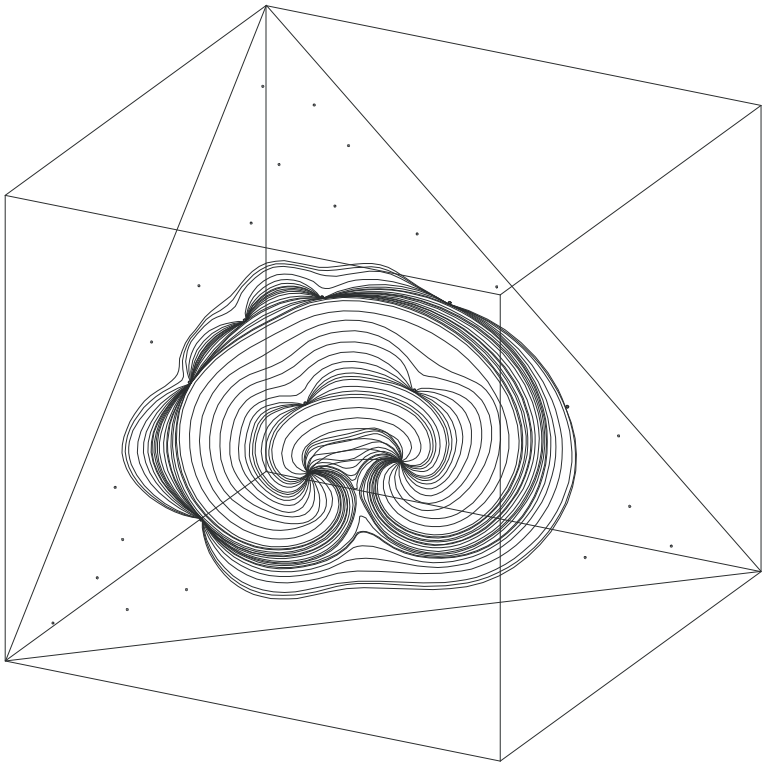

Figure 29: Interaction between a Frank-Read source and discrete barriers in fcc metals.

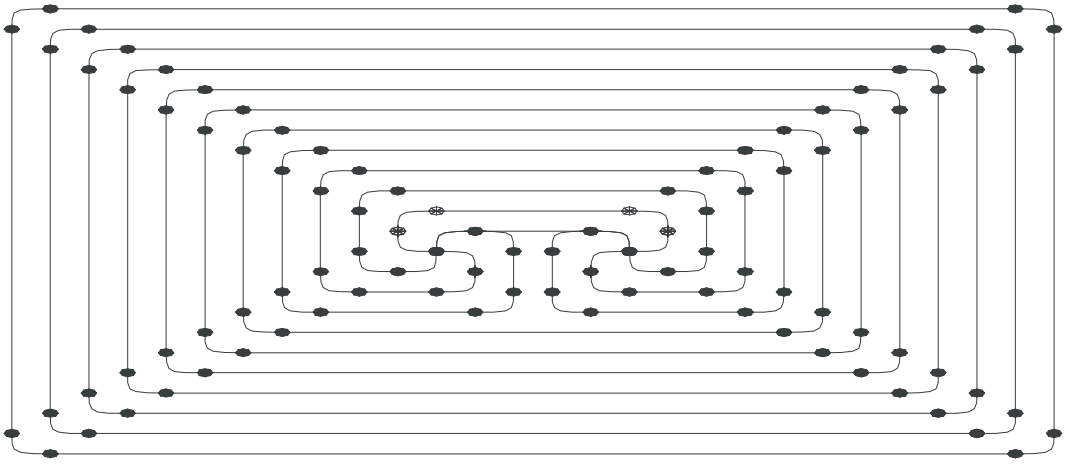

Figure 30: Double-ended Frank-Read source in bcc metals. The straight segments are either screw or edge, while the curved corners are of mixed type.

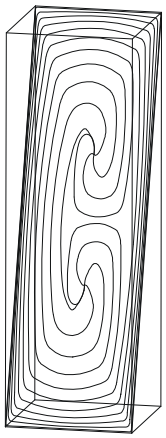

Figure 31: Dislocation loop generation by the Frank-Read mechanism for anisotropic mobility of screw and edge components.

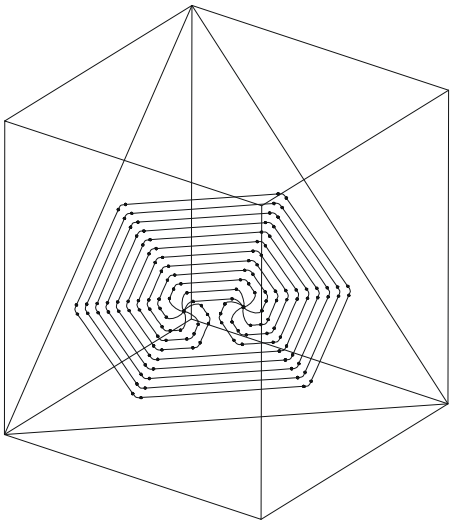

Figure 32: Dislocation generation in covalently-bonded silicon. The directions of the hexagon sides are along $< 111 >$-orientations for screw segments, and $\pm 60^o$ for mixed ones.

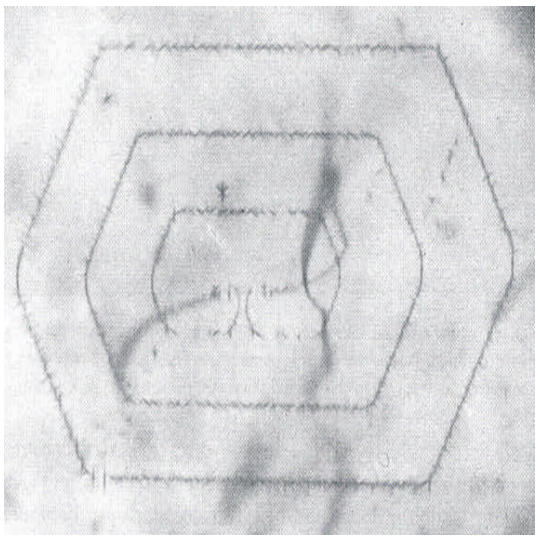

Figure 33: Double-ended Frank-Read source in silicon made visible by copper decoration. Taken from the work of W. C. Dash [92]

low, which leads to a time-step on the order of $0.01s$, similar to the situation in bcc metals [91].

When general cubic spline segments are used, we must solve for tangent vectors at each node, in addition to nodal displacements in order to generate the dislocation loop geometry at successive time-steps. However, for special polygonal loop geometries, additional constraints are needed to maintain accurate loop profiles. For this purpose, we use two types of segments: linear ones for the sides, and curved segments for polygonal corners. The curvature of all nodes is thus constrained to be zero, which guarantees the alignment of polygonal sides to crystallographic directions, as can be seen in Fig. 32. The procedure outlined above produces hexagonal loops with rounded corners, in agreement with the experimental observations on dislocation sources in Si by Dash [92], as can be seen in Figs. 33 and 34.

8.3 Dislocation Loop Interactions

In this section, we illustrate the application of the present parametric method and its associated computational protocols to several problems involving the interaction of dislocation loops. In Fig. 35, two initial screw segments of equal length are assumed to be collinear, and of the same initial length on the [110]-slip plane of a bcc crystal at high temperature, and a high shear stress is applied on the slip plane. Bowing of the two segments is tracked with nodal displacements and tangent vector direction, and the loops are reconstructed by quintic spline segments after each time-step. The process is repeated till any two curved segments on the same loop, or on the two different loops, approach each other. The annihilation criterion is applied, leading to the loop profiles shown in Fig. 35. The applied stress is higher than the maximum value of the self energy after the two loops join one another, because the nodal curvatures are much smaller than corresponding values near the fixed ends of the each loop. Hence, further nodal displacements are not influenced as

Figure 34: Single-ended source of the Frank-Read type in silicon, made visible by copper decoration. Notice the cusps in some of the dislocations. Trails due to defects left behind on moving, are visible behind the cusps. Taken from the work of W. C. Dash [92]

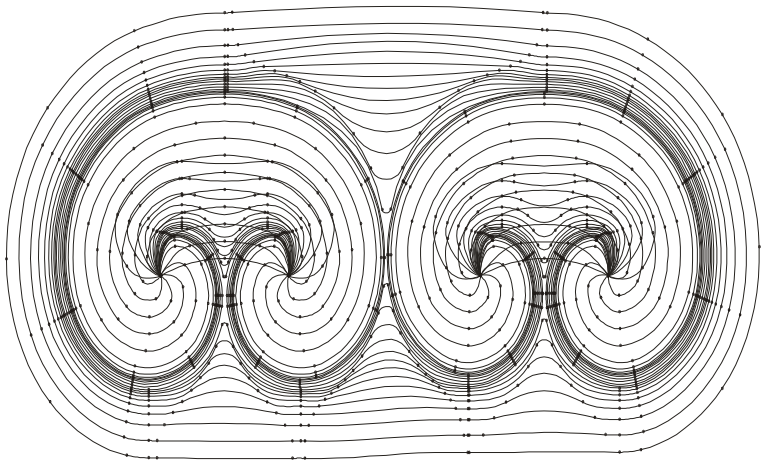

Figure 35: Coplanar dislocation loop interaction

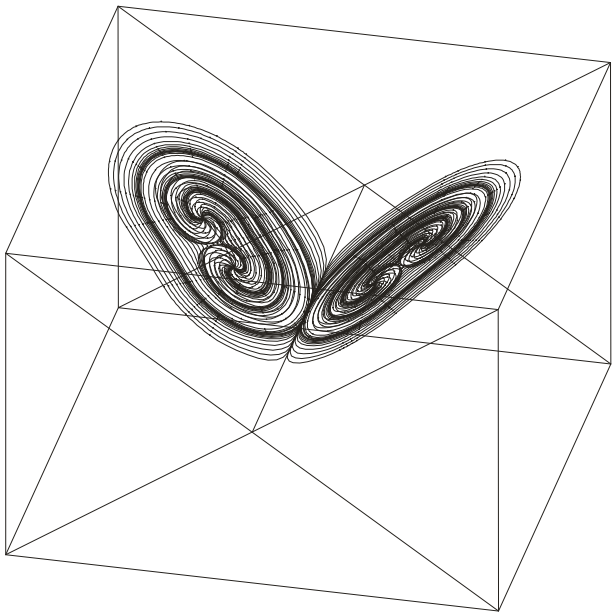

Figure 36: Formation of a dislocation junction in bcc metals

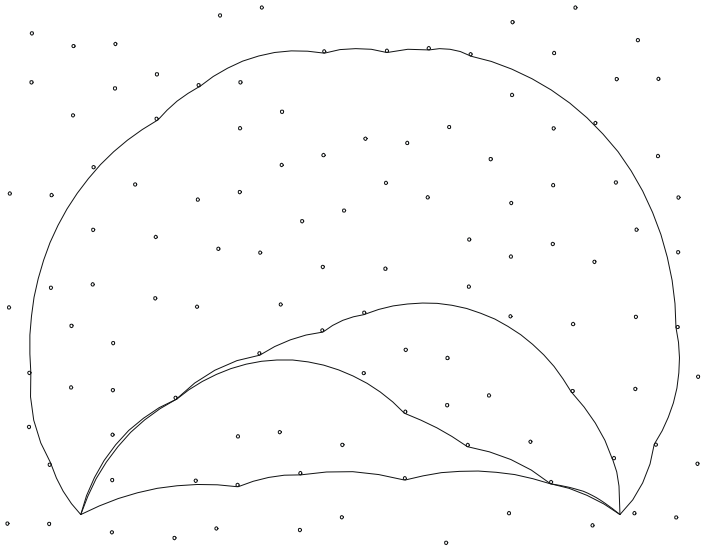

Figure 37: Computer simulation of forest hardening in Cu.

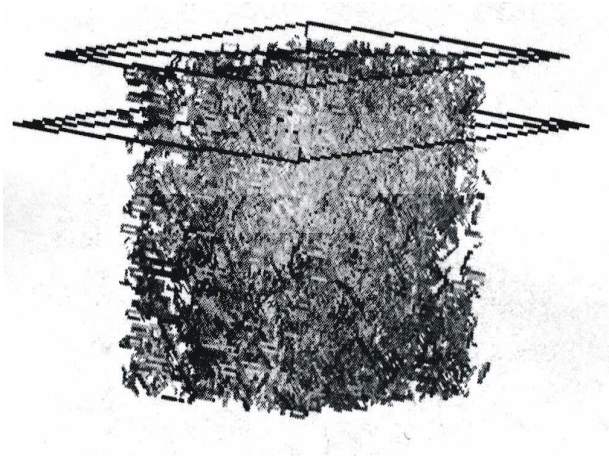

Figure 38: 3-d computer simulation of the initial dislocation microstructure in bcc vanadium. the dislocation density is $10^9 cm^{-2}$.

much with nodal curvatures, once the two loops join together as a single loop. Another illustration of loop-loop interaction is shown in Fig. 36, where two glide loops on different {111}-planes interact and form a sessile junction at the intersection between the two glide planes. In this case, the Burgers vector of the resulting junction does not lie on any of the two slip planes.

Fig. 37 shows the results of computer simulations for the interaction between a slip dislocation on the $< 111 >$-glide plane in copper, after it is emitted from two fixed ends of a Frank-Read source with small defect clusters (Stacking Fault Tetrahedra (SFT)) in irradiated copper single crystals. The dislocation lines represent successive advancement stages under an applied shear stress. The corresponding values of the critical applied shear stress are: 93, 123, 154, and 185 MPa, respectively. A random distribution of SFT is introduced on the glide plane at an average spacing of $20nm$. The dislocation line seeks the nearest SFT and bends around it to a critical angle of $\sim 80^o$ before the obstacle is overcome. This critical angle is higher than the value attributed to dislocation-dislocation intersection in Cu, because the SFT is considered a weak obstacle.

8.4 Dislocation Microstructure Evolution

Computer simulations of dislocation microstructure evolution in bcc metals have been initiated, with the dislocation microstructure represented as dislocation loops inside a three-dimensional cube of 3 micron side-dimensions. Dislocations at low temperature in bcc metals tend to be straight, and mostly screw , and they lie along $< 111 >$-directions. The initial microstructure of a dislocation distribution in a vanadium crystal is shown in Fig. 38, while a *TEM* slice is shown in Fig. 39. the dislocation density is $10^9 cm^{-2}$. As deformation continues, the dislocation density increases, and strain hardening commences.

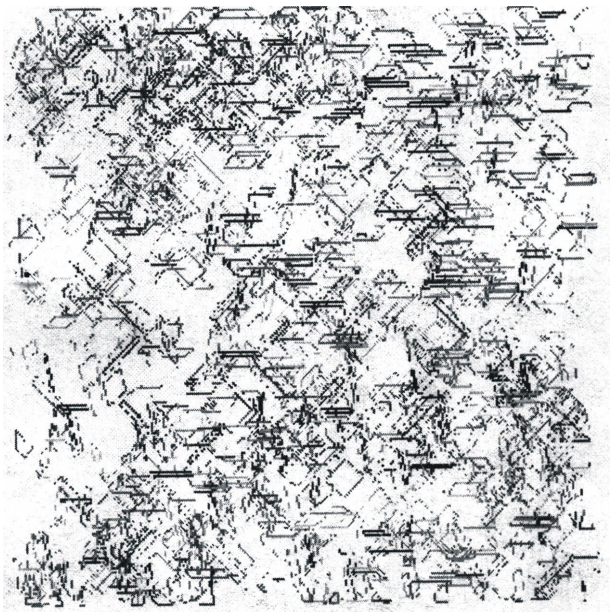

Figure 39: Computer-generated *TEM* -picture of the dislocation structure of Fig. 38.

On-going research is aimed at determination of the stress-strain constitutive relationship from the microstructure shown in Fis. 38, and 39.

9 CONCLUSIONS

The fast sum method, which is based on a combination of dislocation loop geometry parameterization, and numerical quadrature integrations along parameterized curves is shown to be computationally feasible and highly accurate. All calculations involve simple algebraic operations, which can be systematically carried out by straight-forward computer programming. Although we used FORTRAN-90 to implement the results of calculations, even spreadsheets on personal computers can be effectively utilized. The method is as efficient as analytical solutions, especially because of the index structure associated with tensor notation (i.e. the use of DO loops). However, because analytical solutions are available only for a limited number of special cases, the present approach can be used for calculations involving complex loop geometries. The present method is primarily intended for applications in Dislocation Dynamics computer simulations, where the need for accuracy is critical in close-range dislocation encounters. Moreover, one may consider the present method as an extension of the FEM technique in continuum mechanics. A variety of parameterized elements can thus be chosen (in much the same way as in the FEM approach) to handle special dislocation deformation problems. The method may also be exploited in crack problems, where dislocation distributions can be used to represent complex crack surfaces.

To handle the effects of free crystal surfaces on the redistribution of the elastic field inside the crystal, and hence on computed Peach-Kohler forces, the superposition method of Cleveringa et. al. is extended to 3-D applications. While only 2-D problems have

been solved so far by their method, we show that 3-D problems can also be successfully implemented. However, the simple problem shown here required almost 10,000 elements, with an associated large number of degrees of freedom. Other methods (e.g. the Boundary Integral (BI) method) may be more appropriate for 3-D computer simulations, since the stress field should be updated very frequently during Dislocation Dynamics computer simulations

The present method is in the spirit of the Finite Element Method in structural mechanics, where the dislocation line is segmented and described by known shape functions in a linear combination of unknown generalized coordinates, such as position, tangent and normal vectors. Physical arguments are used to ascribe constraints on these generalized coordinates, and thus reduce the number of equations of motion. The method is illustrated in a number of applications on dislocation loop generation and interactions in bcc, fc and dc materials. Many applications of the present method are feasible, especially in areas where continuum descriptions of plastic deformation fall short. One such application is the simulation of the onset of plastic instabilities and the formation of dislocation channels in irradiated materials [57], [94]. It is concluded that the present method offers a number of potential advantages:

1. A natural description of dislocation loop geometry that is not determined by an underlying computational mesh, and which is able to conform to physical constraints imposed by the crystal structure .

2. Avoidance of numerical divergence problems for very short straight segments, and the loss of accuracy on long segments.

3. High resolution of short-range reactions in between curved dislocation segments.

4. Flexibility in mixing segment types during the same computation, thus leading to a reduction in the overall computational burden.

5. Compatibility with the standard Finite Element Method, which may lead to direct coupling with the computational methods of continuum mechanics.

While continuum approaches to constitutive models are limited to the underlying experimental data-base, the present method offers a new direction for modeling microstructure evolution from fundamental principles. The limitation to the method presented here is mainly computational, and much effort is needed to overcome several difficulties. First, the length and time scales represented by the present method are still short of many experimental observations, and methods of rigorous extensions are still needed. Second, the boundary conditions of real crystals are more complicated, especially when external and internal surfaces are to be accounted for. Thus, the present approach does not take into account large lattice rotations, and finite deformation of the underlying crystal, which may be important for explanation of certain scale effects on plastic deformation. And finally, a much expanded effort is needed to bridge the gap between atomistic calculations of dislocation properties on the one hand, and continuum mechanics formulations on the other. Nevertheless, with all of these limitations, the approach presented here is worth

pursuing, because it opens up new possibilities for linking the fundamental nature of the microstructure with realistic material deformation conditions. It can thus provide an additional tool to both theoretical and experimental investigations of plasticity and failure of materials.

Acknowledgments

The author would like to acknowledge the financial support of the US Department of Energy /Office of Fusion Energy through grant number DE-FG03-98ER54500, and Lawrence Livermore National Laboratory through grant numbers B339029, MI-98-031 & MI-99-017, with UCLA. This review is based upon several papers and reports co-authored with a number of students and research associates, to whom the author is deeply grateful. The valuable assistance of Drs. L. Sun, S. Tong and S. Sharafat, and of M. Bacaloni, A. Chen, and R. Sadek is appreciated.

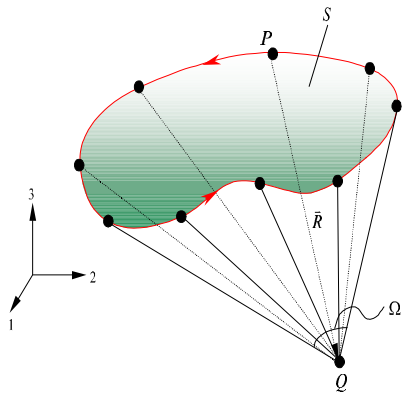

Figure 40: Representation of the solid angle, - , at a field point (Q) away from the dislocation loop line containing the set of points (P)

APPENDICES

A Differential Geometry of the Solid Angle

As shown in Fig. 40, the solid angle differential d- is the ratio of the projected area element $d\mathbf{S}$ to the square of R. Thus:

$$\text{-} = \int d\text{-} = \int_S \frac{\mathbf{e} \bullet d\mathbf{S}}{R^2} = \int_S \frac{X_i dS_i}{R^3} = -\frac{1}{2}\int_S R_{,ppi} dS_i \tag{111}$$

where $\mathbf{e} = \mathbf{R}/R = set\{e_i\}$ is a unit vector along $\mathbf{R} = set\{X_i\}$, and $R_{,ppi} = -2X_i/R^3$. The solid angle can be computed as a line integral, by virtue of Stokes theorem. A vector potential $\mathbf{A}$ **(R)** is introduced by deWit to satisfy the differential equation: $\in_{pik} A_{k,p}(\mathbf{R}) = X_i R^{-3}$. The solution is given by [54]: $A_k(\mathbf{R}) = \in_{ijk} X_i s_j/[R(R + \mathbf{R} \bullet \mathbf{s})]$, where $\mathbf{s}$ is an arbitrary unit vector. This results in non-uniqueness of the displacement field, although it can be arbitrarily symmetrized [73]. The solid angle is then given as a line integral: - $(\mathbf{R}) = \oint_C A_k(\mathbf{R}) d\ell_k$. Taking the derivatives of - in Eq. 111, and applying Eq. 86, we obtain:

$$\text{-}_{,j} = \frac{1}{2}\int_S (R_{,ppll} dS_j - R_{,pplj} dS_l) = \frac{1}{2}\oint_C \in_{jkl} R_{,ppl} dl_k \tag{112}$$

Successive derivatives of the vector $\mathbf{R}$ are given by the following set of equations:

$$\begin{aligned}
R_{,i} &= \frac{X_i}{(X_q X_q)^{\frac{1}{2}}} = \frac{X_i}{R} = e_i \\
R_{,ij} &= \frac{\delta_{ij}}{(X_q X_q)^{\frac{1}{2}}} - \frac{X_i X_j}{(X_q X_q)^{\frac{3}{2}}} = \frac{\delta_{ij}}{R} - \frac{X_i X_j}{R^3} = (\delta_{ij} - e_i e_j)/R \\
R_{,ijk} &= -\frac{\delta_{jk} X_i + \delta_{ik} X_j + \delta_{ij} X_k}{(X_q X_q)^{\frac{3}{2}}} + \frac{3 X_i X_j X_k}{(X_q X_q)^{\frac{5}{2}}}
\end{aligned}$$

$$
\begin{aligned}
&= -\frac{\delta_{jk}X_i + \delta_{ik}X_j + \delta_{ij}X_k}{R^3} + \frac{3X_iX_jX_k}{R^5} \\
&= \left(3e_ie_je_k - [\delta_{ij}e_k + \delta_{jk}e_i + \delta_{ki}e_j]\right)/R^2
\end{aligned} \tag{113}
$$

The third rank tensor R_{ijk} has only 10 non-vanishing terms, and these are given below for convenience.

$$
\begin{aligned}
R_{,111} &= 3e_1({e_1}^2 - 1)/R^2, \qquad R_{,112} = e_2(3e_1^2 - 1)/R^2 \\
R_{,113} &= e_3(3e_1^2 - 1)/R^2, \qquad R_{,221} = e_1(3e_2^2 - 1)/R^2 \\
R_{,222} &= 3e_2(e_2^2 - 1)/R^2, \qquad R_{,223} = e_3(3e_2^2 - 1)/R^2 \\
R_{,331} &= e_1(3e_3^2 - 1)/R^2, \qquad R_{,332} = 3e_2(3e_3^2 - 1)/R^2 \\
R_{,333} &= 3e_3(e_3^2 - 1)/R^2, \qquad R_{,123} = 3e_1e_2e_3/R^2
\end{aligned} \tag{114}
$$

B The Displacement Field and Green's Functions

Define Greens function: $U_{ij}(\mathbf{R})$, as the displacement component $U_i(\mathbf{r})$ at position $(\mathbf{R})$ due to point force in the R_j-direction at the origin. It can be obtained by considering the equation of translational equilibrium, that is:

$$C_{ijkl}u_{k,lj} + f_i = 0 \tag{115}$$

If the point force is in the m-direction, it can be represented by:

$$f_i = \delta_{im}\delta(\mathbf{r}) \tag{116}$$

Where the Dirac-delta function is $\delta(\mathbf{r}) = \delta(r_1)\delta(r_2)\delta(r_3)$, with the property:

$$\int_V \delta(\mathbf{r} - \hat{\mathbf{r}})f(\hat{\mathbf{r}})\ dV = f(\mathbf{r})$$

Translational equilibrium is satisfied by:

$$C_{ijkl}U_{k,lj} + \delta_{im}\delta(\mathbf{r}) = 0 \tag{117}$$

Given a point force distribution $f_m(\mathbf{r})$, the corresponding displacement vector distribution is obtained as:

$$u_i(\mathbf{r}) = \int_{allspace} U_{km}(\mathbf{r} - \hat{\mathbf{r}})f_m(\hat{\mathbf{r}})\ d\hat{V} \tag{118}$$

However, for a finite region of space, we use the divergence theorem for any rank tensor $\mathbf{T}$ is expressed as:

$$\int_V \nabla \bullet \mathbf{T}\ dV = \int_S \mathbf{T}\bullet\ d\mathbf{S} = \int_V \mathbf{T}_{,i}dV = \int_S \mathbf{T}dS_i$$

Now consider the following equation:

$$\begin{aligned}
\int_{\hat{V}} C_{ijkl}\left[u_i(\hat{\mathbf{r}})U_{km,\hat{l}\hat{j}} - U_{im}(\mathbf{r}-\hat{\mathbf{r}})u_{k,\hat{l}\hat{j}}(\hat{\mathbf{r}})\right]\ d\hat{V} = \\
= \int_{\hat{S}} C_{ijkl}\left[u_i(\hat{\mathbf{r}})U_{km,\hat{l}} - U_{im}u_{k,\hat{l}}(\hat{\mathbf{r}})\right]\ dS_{\hat{j}} \\
= \int_{\hat{V}} \left[-u_i(\hat{\mathbf{r}})\delta_{ij}\delta(\mathbf{r}-\hat{\mathbf{r}}) + U_{im}f_i\right]\ d\hat{V} \\
= \int_{\hat{S}} \left[u_i(\hat{\mathbf{r}})C_{ijkl}U_{km,\hat{l}} - U_{im}\sigma_{ij}(\hat{\mathbf{r}})\right]\ dS_{\hat{j}} \qquad (119)
\end{aligned}$$

Re-arranging terms, we can easily determine the displacement vector anywhere, given that a distributed force system is specified in the volume, and that stress and displacement conditions are prescribed at the boundary. Hence, we have:

$$u_m(\mathbf{r}) = \int_{\hat{V}} U_{im}(\mathbf{r}-\hat{\mathbf{r}})\, f_i(\hat{\mathbf{r}})\, d\hat{V} - \int_{\hat{S}} u_i(\hat{\mathbf{r}})\, C_{ijkl}U_{km,\hat{l}}(\mathbf{r}-\hat{\mathbf{r}})\, d\hat{S}_j + \int_{\hat{S}} U_{im}(\mathbf{r}-\hat{\mathbf{r}})\, \sigma_{ij}(\hat{\mathbf{r}})\, d\hat{S}_j \qquad (120)$$

The second and third terms in Eq.120 account for displacement and traction boundary conditions on the surface $\hat{S}$, respectively. The specific case of a dislocation loop is characterized by the absence of body forces within the volume (i.e. $f_i = 0$), zero tract ions on the boundary (i.e. $\sigma_{ij} = 0$) on $\hat{S}$, and a rigid displacement vector b_i across the surface $\hat{S}$. The displacement equation is finally given by:

$$u_m(\mathbf{r}) = -b_i \int_{\hat{S}} C_{ijkl}U_{km,\hat{l}}(\mathbf{r}-\hat{\mathbf{r}})\, d\hat{S}_j = b_i \int_{\hat{S}} C_{ijkl}U_{km,l}(\mathbf{r}-\hat{\mathbf{r}})\, d\hat{S}_j \qquad (121)$$

To complete determination of the displacement field, we need to evaluate Green's functions of isotropic elasticity, as given below. We use the method of Fourier transform, defined as:

$$\tilde{U}_{km}(\mathbf{k}) = \int_V U_{km}(\mathbf{r})\, e^{-i\mathbf{k}\cdot\mathbf{r}} dV$$

with its inverse:

$$U_{km}(\mathbf{r}) = \frac{1}{(2\pi)^3} \int_{V_k} \tilde{U}_{km}(\mathbf{k})\, e^{i\mathbf{k}\cdot\mathbf{r}} dV_k$$

and the associated differentiation rules:

$$k_l\tilde{U}_{km} = \int_V U_{km,l}(\mathbf{r}) e^{-i\mathbf{k}\cdot\mathbf{r}} dV \qquad (122)$$

$$-k_lk_j\tilde{U}_{km} = \int_V U_{km,lj}(\mathbf{r}) e^{-i\mathbf{k}\cdot\mathbf{r}} dV \qquad (123)$$

We start now from the equilibrium equation, and take its Fourier transform:

$$\begin{aligned}
C_{ijkl}U_{km,lj} &= -\delta_{im}\delta(\mathbf{r}) \\
-C_{ijkl}k_lk_j\tilde{U}_{km}(\mathbf{k}) &= -\delta_{im} \qquad (124)
\end{aligned}$$

For an isotropic elastic solid, we have:

$$\begin{aligned} \mu\left(\delta_{ik}\delta_{jl}+\delta_{il}\delta_{jk}\right)k_l k_j \tilde{U}_{km}(\mathbf{k}) + \lambda\delta_{ij}\delta_{kl}k_l k_j \tilde{U}_{km}(\mathbf{k}) &= \delta_{im} \\ \mu\delta_{ik}\delta_{jl}k_l k_j \tilde{U}_{km}(\mathbf{k}) + \mu\delta_{il}\delta_{jk}k_l k_j \tilde{U}_{km}(\mathbf{k}) + \lambda\delta_{ij}\delta_{kl}k_l k_j \tilde{U}_{km}(\mathbf{k}) &= \delta_{im} \end{aligned} \tag{125}$$

Using the substitution property of the delta function, we obtain:

$$\begin{aligned} \mu\delta_{ik}\delta_{jl}k_l k_j \tilde{U}_{km}(\mathbf{k}) &= \mu k_l k_l \tilde{U}_{im}(\mathbf{k}) \\ \mu\delta_{il}\delta_{jk}k_l k_j \tilde{U}_{km}(\mathbf{k}) = \mu k_i k_j \tilde{U}_{jm}(\mathbf{k}) &= \mu k_i k_k \tilde{U}_{km}(\mathbf{k}) \end{aligned} \tag{126}$$

Now, exchange $j \rightarrow k$:

$$\lambda\delta_{ij}\delta_{kl}k_l k_j \tilde{U}_{km}(\mathbf{k}) = \lambda k_l k_i \tilde{U}_{lm}(\mathbf{k}) = \lambda k_i k_k \tilde{U}_{km}\mathbf{k}) \tag{127}$$

And exchange $l \rightarrow k$:

$$(\mu+\lambda)k_k k_i \tilde{U}_{km} + \mu k^2 \tilde{U}_{im} = \delta_{im} \tag{128}$$

Then, multiply by k_i and sum over i:

$$\begin{aligned} (\mu+\lambda)k_k k_i k_i \tilde{U}_{km} + \mu k^2 k_i \tilde{U}_{im} &= \delta_{im}k_i \\ (\mu+\lambda)k_k k^2 \tilde{U}_{km} + \mu k^2 k_i \tilde{U}_{im} &= k_m \end{aligned} \tag{129}$$

Exchange $i \leftarrow k$, and re-arrange:

$$\begin{aligned} (\mu+\lambda)k_k k^2 \tilde{U}_{km} + \mu k^2 k_k \tilde{U}_{km} &= k_m \\ (2\mu+\lambda)k_k k^2 \tilde{U}_{km} &= k_m \qquad \text{or,} \\ k_k \tilde{U}_{km} &= \frac{k_m}{(2\mu+\lambda)k^2} \end{aligned} \tag{130}$$

This result can now be substituted back into Eq. 128 above. The elastic Green's functions are readily obtained in Fourier space as:

$$\begin{aligned} \left(\frac{\mu+\lambda}{2\mu+\lambda}\right)\frac{k_i k_m}{k^2} + \mu k^2 \tilde{U}_{im} &= \delta_{im} \\ \tilde{U}_{im}(\mathbf{k}) &= \frac{1}{\mu}\left[\frac{\delta_{kim}}{k^2} - \left(\frac{\mu+\lambda}{2\mu+\lambda}\right)\frac{k_k k_m}{k^4}\right] \end{aligned} \tag{131}$$

To obtain the elastic Green's functions in Cartesian space, we use the following properties of the inverse Fourier transform:

$$\frac{1}{\pi^2}\int\limits_{V_k} \frac{e^{i\mathbf{k}\cdot\mathbf{r}}}{k^4} dV_k = -r \tag{132}$$

And its second derivative:

$$\frac{1}{\pi^2}\int\limits_{V_k} \frac{k_m k_m e^{i\mathbf{k}\cdot\mathbf{r}}}{k^4} dV_k = r_{,km} \tag{133}$$

While for $k = m = p$, we have:

$$\frac{1}{\pi^2} \int\limits_{V_k} \frac{e^{i\mathbf{k}\cdot\mathbf{r}}}{k^2} dV_k = r_{,pp} \tag{134}$$

Finally, we can now use Eqs. 133 and 134, and take the inverse Fourier transform of Eq. 131 to obtain the explicit form of the isotropic elastic Green's functions:

$$U_{km}\left(\mathbf{r}\right) = \frac{1}{8\pi\mu}\left[\delta_{km} r_{,pp} - \left(\frac{\lambda+\mu}{\lambda+2\mu}\right) r_{,km}\right] \tag{135}$$

Similarly, the Green's functions $U_{km}(\mathbf{r} - \hat{\mathbf{r}}) = U_{km}(\mathbf{R})$, and their derivative with respect to l are given by:

$$\begin{aligned} U_{km}\left(\mathbf{R}\right) &= \frac{1}{8\pi\mu}\left[\delta_{km} R_{,pp} - \left(\frac{\lambda+\mu}{\lambda+2\mu}\right) R_{,km}\right] \\ U_{km,l}\left(\mathbf{R}\right) &= \frac{1}{8\pi\mu}\left[\delta_{km} R_{,ppl} - \left(\frac{\lambda+\mu}{\lambda+2\mu}\right) R_{,kml}\right] \end{aligned} \tag{136}$$

C Burgers Equation

Burgers equation is a fundamental line integral, which will also be utilized in determination of all elastic field variables by the computational fast sum method. Our purpose here is to derive the displacement vector of a dislocation loop as a line integral. Let's now substitute Eq. 136 for Green's function derivatives, and Eq. 81 for the isotropic values of the elastic constants into the surface integral in Eq. 84 to obtain:

$$u_m(\mathbf{r}) = \frac{1}{8\pi\mu} \int\limits_{\hat{S}} \left[\lambda b_i \delta_{ij} \delta_{kl} + \mu\left(b_i \delta_{ik} \delta_{jl} + b_i \delta_{il} \delta_{jk}\right)\right] \left[\delta_{km} R_{,ppl} - \left(\frac{\lambda+\mu}{\lambda+2\mu}\right) R_{,kml}\right] d\hat{S}_j \tag{137}$$

recall the substitution property of the Kronecker delta function: $b_i \delta_{ij} = b_j$, $b_i \delta_{ik} = b_k$, $b_i \delta_{il} = b_l$, Eq. 88 takes the form:

$$\begin{aligned} u_m(\mathbf{r}) = \frac{1}{8\pi\mu} \int\limits_{\hat{S}} \{&\lambda b_j \delta_{kl} \delta_{km} R_{,ppl} + \mu(b_k \delta_{jl} \delta_{km} R_{,ppl} + b_l \delta_{jk} \delta_{km} R_{,ppl}) - \\ &(\frac{\lambda+\mu}{\lambda+2\mu})[\lambda b_j \delta_{kl} R_{,kml} + \mu(b_k \delta_{jl} R_{,kml} + b_l \delta_{jk} R_{,kml})]\} d\hat{S}_j \end{aligned} \tag{138}$$

We will now utilize the following tensor properties:

$$\begin{aligned} b_j \delta_{kl} \delta_{km} R_{,ppl} &= b_j R_{,ppm} \\ b_j \delta_{kl} R_{,kml} &= b_j R_{,llm} \\ b_k \delta_{jl} \delta_{km} R_{,ppl} + b_l \delta_{jk} \delta_{km} R_{,ppl} &= b_m R_{,ppj} + b_l \delta_{jm} R_{,ppl} \\ b_k \delta_{jl} R_{,kml} + b_l \delta_{jk} R_{,kml} &= b_k R_{,kmj} + b_l R_{,jml} \end{aligned} \tag{139}$$

$$\begin{aligned} u_m(\mathbf{r}) = \frac{1}{8\pi\mu} \int\limits_{\hat{S}} \{&\lambda b_j R_{,ppm} + \mu(b_m R_{,ppj} + b_l \delta_{jm} R_{,ppl}) - \\ &(\frac{\lambda+\mu}{\lambda+2\mu})[\lambda b_j R_{,llm} + \mu(b_k R_{,kmj} + b_l R_{,jml})]\} d\hat{S}_j \end{aligned} \tag{140}$$

For any rank tensor, recall Stokes theorem: $\int\limits_S (\nabla \times \mathbf{T}) \bullet d\mathbf{S} = \oint\limits_C \mathbf{T} \bullet d\ell$. Since: $\nabla \times \mathbf{T} = \in_{ijk} T_{abc\cdots,i} e_k$, we have:

$$\int\limits_S (\nabla \times \mathbf{T}) \bullet d\mathbf{S} = \int\limits_S \in_{ijk} T_{abc\cdots,i} e_k dS_r \; e_r = \int\limits_S \in_{ijk} T_{abc\cdots,i} \delta_{kr} dS_r = \int\limits_S \in_{ijk} T_{abc\cdots,i} dS_k$$

Thus, Stokes theorem can be used to convert a surface integral into a line integral as:

$$\int\limits_S \in_{ijk} T_{abc\cdots,i} dS_k = \oint\limits_C T_{abc\cdots} dl_j \tag{141}$$

Multiplying both sides by $\in_{klm}$, and utilizing the tensor property:$\in_{ijk} \in_{klm} = \delta_{il}\delta_{jm} - \delta_{im}\delta_{jl}$, we have:

$$\begin{aligned} \int\limits_S (\delta_{il}\delta_{jm} - \delta_{im}\delta_{jl}) \, T_{abc\cdots,j} dS_i &= \oint\limits_C \in_{lmj} T_{abc\cdots} dl_j \\ \int\limits_S (T_{abc\cdots,m} dS_l - T_{abc\cdots,l} dS_m) &= \oint\limits_C \in_{klm} T_{abc\cdots} dl_k \end{aligned} \tag{142}$$

Or, expressed in the *hat* coordinates, we have:

$$\int\limits_{\hat{S}} \left(T_{abc\cdots,m} d\hat{S}_l - T_{abc\cdots,l} d\hat{S}_m \right) = \oint\limits_C \in_{klm} T_{abc\cdots} d\hat{l}_k \tag{143}$$

Rewriting Eq. 137, the expression can be manipulated and rearranged in the following form:

$$\begin{aligned} u_m(\mathbf{r}) = \frac{1}{8\pi} \int\limits_{\hat{S}} b_m R_{,ppj} d\hat{S}_j &+ \frac{1}{8\pi} \int\limits_{\hat{S}} (b_l R_{,ppl} d\hat{S}_m - b_j R_{,ppm} d\hat{S}_j) \\ &+ \frac{1}{4\pi} \left(\frac{\lambda + \mu}{\lambda + 2\mu}\right) \int\limits_{\hat{S}} (b_j R_{,ppm} d\hat{S}_j - b_k R_{,kmj} d\hat{S}_j) \end{aligned} \tag{144}$$

Applying Eq. 143 to the third order tensor $R_{,ijk}$, we obtain the following:

$$\begin{aligned} \int\limits_S [b_l R_{,ppl} dS_m - b_j R_{,ppm} dS_j] &= \oint\limits_C \in_{klm} b_l R_{,pp} dl_k \\ \int\limits_S [b_j R_{,ppm} dS_j - b_n R_{,\min} dS_i] &= \oint\limits_C \in_{kin} b_n R_{,mi} dl_k \end{aligned} \tag{145}$$

Finally, when we substitute from Eqns. 111 and 145 into Eq. 144, we obtain the line integral form of Burgers equation, given by Eq. 85.

D Stress tensor components

For one loop, explicit fast sum forms of the 3-dimensional stress tensor components are given below. The inner sum is extended over the number of quadrature points assigned

in the interval $-1 \leq \hat{u}l0$. Q_{max} is typically 8-16 for accurate results, although cases with Q_{max} up to 300 have been tested. The outer sum is over the number of loop segments, which is typically in the range 10-30. For an arbitrary number of loops of defined parametric geometry, a third sum over the loop number must additionally be included.

$$\sigma_{11} = \frac{\mu}{8\pi} \sum_{\gamma=1}^{N_{loop}} \sum_{\beta=1}^{N_s} \sum_{\alpha=1}^{Q_{max}} w_\alpha \left\{ \begin{array}{l} \left[b_2 \left(-2R,_{113} + \frac{2\nu}{1-\nu} \left(R,_{223} + R,_{333} \right) \right) + b_3 \left(2R,_{112} - \frac{2\nu}{1-\nu} \left(R,_{222} + R,_{332} \right) \right) \right] \hat{r}_{1,u} + \\ \left[-b_1 \frac{2}{1-\nu} \left(R,_{223} + R,_{333} \right) + b_3 \frac{2}{1-\nu} \left(R,_{221} + R,_{331} \right) \right] \hat{r}_{2,u} + \\ \left[+b_1 \frac{2}{1-\nu} \left(R,_{222} + R,_{332} \right) - b_2 \frac{2}{1-\nu} \left(R,_{221} + R,_{331} \right) \right] \hat{r}_{3,u} \end{array} \right\}_\alpha \tag{146}$$

$$\sigma_{12} = \frac{\mu}{8\pi} \sum_{\gamma=1}^{N_{loop}} \sum_{\beta=1}^{N_s} \sum_{\alpha=1}^{Q_{max}} w_\alpha \left\{ \begin{array}{l} \left[b_1 \left(R,_{113} + R,_{223} + R,_{333} \right) - b_2 \left(\frac{2}{1-\nu} R,_{123} \right) + b_3 \left(\frac{1+\nu}{1-\nu} R,_{221} - R,_{111} - R,_{331} \right) \right] \hat{r}_{1,u} + \\ \left[b_1 \left(\frac{2}{1-\nu} R,_{123} \right) - b_2 \left(R,_{113} + R,_{223} + R,_{333} \right) + b_3 \left(-\frac{1+\nu}{1-\nu} R,_{112} + R,_{222} + R,_{332} \right) \right] \hat{r}_{2,u} + \\ \frac{2}{1-\nu} \left(-b_1 R,_{221} + b_2 R,_{112} \right) \hat{r}_{3,u} \end{array} \right\}_\alpha \tag{147}$$

$$\sigma_{13} = \frac{\mu}{8\pi} \sum_{\gamma=1}^{N_{loop}} \sum_{\beta=1}^{N_s} \sum_{\alpha=1}^{Q_{max}} w_\alpha \left\{ \begin{array}{l} \left[-b_1 \left(R,_{112} + R,_{222} + R,_{332} \right) + b_2 \left(R,_{111} + R,_{221} - \frac{1+\nu}{1-\nu} R,_{331} \right) + b_3 \left(\frac{2}{1-\nu} R,_{123} \right) \right] \hat{r}_{1,u} + \\ \frac{2}{1-\nu} \left(b_1 R,_{331} - b_3 R,_{113} \right) \hat{r}_{2,u} + \\ \left[-b_1 \left(\frac{2}{1-\nu} R,_{123} \right) - b_2 \left(-\frac{1+v}{1-\nu} R,_{113} + R,_{223} + R,_{333} \right) + b_3 \left(R,_{112} + R,_{222} + R,_{332} \right) \right] \hat{r}_{3,u} \end{array} \right\}_\alpha \tag{148}$$

$$\sigma_{22} = \frac{\mu}{8\pi} \sum_{\gamma=1}^{N_{loop}} \sum_{\beta=1}^{N_s} \sum_{\alpha=1}^{Q_{max}} w_\alpha \left\{ \begin{array}{l} \left[b_2 \frac{2}{1-\nu} \left(R,_{113} + R,_{333} \right) - b_3 \frac{2}{1-\nu} \left(R,_{112} + R,_{332} \right) \right] \hat{r}_{1,u} + \\ \left[b_1 \left[-\frac{2\nu}{1-\nu} \left(R,_{113} + R,_{333} \right) + 2R,_{223} \right] + b_3 \left[\frac{2\nu}{1-\nu} \left(R,_{111} + R,_{331} \right) - 2R,_{221} \right] \right] \hat{r}_{2,u} + \\ \left[b_1 \frac{2}{1-\nu} \left(R,_{112} + R,_{332} \right) - b_2 \frac{2}{1-\nu} \left(R,_{111} + R,_{331} \right) \right] \hat{r}_{3,u} \end{array} \right\}_\alpha \tag{149}$$

$$\sigma_{23} = \frac{\mu}{8\pi} \sum_{\gamma=1}^{N_{loop}} \sum_{\beta=1}^{N_s} \sum_{\alpha=1}^{Q_{max}} w_\alpha \left\{ \begin{array}{l} \left[-b_2 \frac{2}{1-\nu} R,_{332} + b_3 \frac{2}{1-\nu} R,_{223} \right] \hat{r}_{1,u} + \\ \left[b_1 \left(-R,_{112} - R,_{222} + \frac{1+\nu}{1-\nu} R,_{332} \right) + b_2 \left(R,_{111} + R,_{221} + R,_{331} \right) - b_3 \left(\frac{2}{1-\nu} R,_{123} \right) \right] \hat{r}_{2,u} + \\ \left[b_1 \left(R,_{113} + R,_{333} - \frac{1+\nu}{1-\nu} R,_{223} \right) + b_2 \left(\frac{2}{1-\nu} R,_{123} \right) - b_3 \left(R,_{111} + R,_{221} + R,_{331} \right) \right] \hat{r}_{3,u} \end{array} \right\}_\alpha \tag{150}$$

$$\sigma_{33} = \frac{\mu}{8\pi} \sum_{\gamma=1}^{N_{loop}} \sum_{\beta=1}^{N_s} \sum_{\alpha=1}^{Q_{max}} w_\alpha \left\{ \begin{array}{l} \left[+b_2 \frac{2}{1-\nu} \left(R,_{113} + R,_{223} \right) - b_3 \frac{2}{1-\nu} \left(R,_{112} + R,_{222} \right) \right] \hat{r}_{1,u} + \\ \left[-b_1 \frac{2}{1-\nu} \left(R,_{113} + R,_{223} \right) + b_3 \frac{2}{1-\nu} \left(R,_{111} + R,_{221} \right) \right] \hat{r}_{2,u} + \\ \left[+b_1 \left[\frac{2\nu}{1-\nu} \left(R,_{112} + R,_{222} \right) - 2R,_{332} \right] + b_2 \left[-\frac{2\nu}{1-\nu} \left(R,_{111} + R,_{221} \right) + 2R,_{331} \right] \right] \hat{r}_{3,u} \end{array} \right\}_\alpha \tag{151}$$

REFERENCES

1. R. J. Amodeo and N. M. Ghoniem, *Res Mechanica*, **23**, 137 (1988).
2. H. Mughrabi, *Acta Metall.*, **31**(9), 1367 (1983).
3. H. Mughrabi, *Mat. Sci. Eng.*, **85**, 15 (1987).
4. L. P. Kubin, Dislocation Patterning, In *Treatises in Materials Science and Technology*, Ed. R. W. Cahn et al., Weinhum, Germany (1993).
5. J. Kratochvil and M. Saxlova, *Solid State Phenomena*, **23/24**, 369 (1992).
6. G. Ananthakrishna, *Solid State Phenomena*, **23/24**, 417 (1992).
7. G. Ananthakrishna, C. Fressengeas, M. Grosbras, J. Vergnol, C. Engelke, C. Plessing, H. Neuhauser, E. Bouchaud, J. Planes, and L. P. Kubin, *Scripta Metallurgica et Materialia*, **32**, 1731 (1995).
8. M. Zaiser, M. Avlonitis, and E.C. Aifantis, *Acta Materialia*, **46**, 4143 (1998).
9. P. Hahner, K. Bay, M. Zaiser, *Phy. Rev. Lett.*, **81**(12), 2470 (1998).
10. V. Gregor, J. Kratochvil, *Inter. J. Plasticity*, **14**, 159 (1998).
11. U. F. Kocks, A.S. Argon, and M. M. Ashby, *Thermodynamics and Kinetics of Slip*. In Progress in Materials Science, Eds. B. Chalmers, J. W. Christian and T. B. Massaiski, Pergamon Press, Oxford, **19**, 1 (1975).
12. N. M. Ghoniem, J. R. Matthews, and R. J. Amodeo, *Res Mechanica*, **29**, 197 (1990).
13. D. Walgraef and E. Aifantis, *J. Appl. Phys.*, **58**, 688 (1985).
14. D. Holt, *J. Appl. Phys.*, **41**, 3197 (1970).
15. F.R.N. Nabarro, *Theory of Crystal Dislocations*, **Oxford at the Clarendon Press**, Oxford, England, (1967)
16. J.P. Hirth and J. Lothe, *Theory of Dislocations*, 2^{2d} edn. **McGraw-Hill**, New York (1982).
17. R. Bullough and R.C. Newman, *Phil. Mag.*, **5**, 921 (1960).
18. E. Kröner, *Kontinuumstheorie der Versetzungen und Eigenspannungen*, **Springer**, Berlin, Germany, (1958).
19. F. Kroupa, *Czech. J. Phys.*, **B 10**, 284 (1960).
20. F. Kroupa, in *Theory of Crystal Defects*, edited by B. Gruber, (Academia Publishing House, Prague), 275 (1966).
21. R. deWit, *Sol. State Phys.*, **10**, 269 (1960).
22. J. Lepinoux and L. P. Kubin, *Scripta Met.*, **21**, 833 (1987).

23. N. M. Ghoniem and R. Amodeo, *Solid State Phenomena*, **3& 4**, 377 (1988).

24. A. N. Guluoglu , D. J. Srolovitz,R. LeSar and R. S. Lomdahl, *Scripta Met.*, **23**, 1347 (1989).

25. N. M. Ghoniem and R. J. Amodeo, In *Patterns, Defects and Material Instabilities*, Eds. D. Walgreaf and N. M. Ghoniem, Kluwer Academic Publishers, Dordrecht, p. 303 (1990).

26. R. J. Amodeo and N. M. Ghoniem, *Phys. Rev. B*, **41**,6958 (1990).

27. R. J. Amodeo and N. M. Ghoniem, *Phys. Rev. B*, **41**, 6968 (1990).

28. R.J. Amodeo and N.M. Ghoniem, "Rapid Algorithms for Dislocation of Dynamics in Micromechanical Calculations," In *Modeling of Deformation of Crystalline Solids*, Eds. T. Lowe, T. Rollett, P. Follansbee, and G. Daehn, TMS Press, p. 125 (1991).

29. I. Groma and G. S. Pawley, *Phil. Mag. A*, **67 (6)**, 1459 (1993).

30. V. A. Lubarda, I. A. Blume, and A. Needleman, *Acta Metall. Mater.*, **41**, 625 (1993).

31. H. Y. Wang and R. Lesar, *Phil. Mag. A*, **71(l)**, 149 (1995).

32. D.B. Barts, A.E. Carlsson, *Phys. Rev. E* , **52** (3, pt.B), 3195 (1995).

33. Cleveringa, H, E. van der Giessen, and A. Needleman,*Journal de Physique IV*, France, **8**(4), 83 (1998).

34. D. Raabe, *Phil. Mag. A* , **77**(3), 751 (1998).

35. L.P. Kubin, G. Canova, M. Condat, B. Devincre, V. Pontikis, and Y. Brechet, *Sol. State Phenomena*, **23/24**, 445 (1992).

36. B. Devincre and M. Condat, *Acta Metall. Mater.*, **40**, 2629 (1992).

37. B. Devinere, V. Pontikis, Y. Brechet, G. Canova, M. Condat, and L. P. Kubin, in *Microscopic Simulations of Complex Hydrodynamic Phenomena*, Ed. M. Mareschal and B. L. Lolian, Plenum Press, New York, p. 413 (1992).

38. G. Canova, Y. Brechet, and L. P. Kubin, In *Modeling of Plastic Deformation and its Engineering Applications*, Eds. S. I. Anderson et al., RISØ National Laboratory, Roskilde, Denmark (1992).

39. L. P. Kubin and G. Canova, *Scripta Metall.*, **27**, 957 (1992).

40. L. P. Kubin, *Phys. Status Solidi (a)*, **135**, 433 (1993).

41. G. Canova, Y. Brechet, L. P. Kubin,B. Devincre, V. Pontikis and M. Condat, *Microstructures and Physical Properties*, Ed J Rabiet, **CH-Transtech** (1993).

42. B. Devincre and L. P. Kubin, *Model. Simul. Mater. Sci. Eng.*, **2**, 559 (1994).

43. B. Devincre, Meso-scale Simulation of the Dislocation Dynamics, In *Computer Simulation in Materials Science*, Eds. H. 0. Krichner et al., Kluwer Academic Press, Dordrecht, p. 309 (1996).

44. B. Devincre, L. Kubin,*Philosophical Transactions of the Royal Society London, Series A (Mathematical, Physical and Engineering Sciences), UK*, **355**(1731), 2003 (1997).

45. A.M. Moulin, P. Condat, L. Kubin, *Acta Mater.*, **45**(6), 2339 (1997).

46. J. P. Hirth, M. Rhee, and H. Zbib, *J. Computer-Aided Mater. Design*, **3**, 164 (1996).

47. K. W. Schwarz and J. Tersoff, *Appl. Phys. Lett.*, **69**, 1220 (1996).

48. K.W. Schwarz, *Phys. Rev. Lett.*,**78**, 4785 (1997).

49. K.W. Schwarz and LeGoues, *Phys. Rev. Lett.*,**79**, 1877 (1997).

50. H.M. Zbib, M. Rhee , and J.P. Hirth, *Int. J. Mech. Sci.*, **40**, 113 (1998).

51. D.C. Chrzan, M. S. Daw, *Phys. Rev. B* , **55**(2), 798 (1997).

52. L. M. Brown, *Phil. Mag.*, **15**, 363 (1967).

53. T. Mura, *Micro Mechanics of Defects in Solids*, **Martinus Nijhoff Publishers**, The Hague, Netherlands, (1982).

54. R. deWit, "The displacement field of a dislocation distribution," in *Dislocation Modeling of Physical Systems*, Eds. M.F. Ashby, R. Bullough, C.S. Hartley and J.P. Hirth, **Pergamon Press**, Oxford, 305 (1980).

55. N.M. Ghoniem, *J. Eng. Mat. Tech.*, **121, No. 2**, 136 (1999).

56. N.M. Ghoniem and L. Z. Sun, *Phys. Rev. B*, **60, No.1**, 128 (1999).

57. N.M. Ghoniem and M. Bacaloni, "Finite Segment Method for 3-D Dislocation Dynamics," Eng. Report No. **UCLA/MATMOD-97-01**, (1997).

58. D. Kuhlmann-Wilsdorf, *Mater. Sci. Eng.* **86**, 53 (1987).

59. L. Yumen and Z. Huijiu, *Mater. Sci. Eng.* **81**, 451 (1986).

60. K. Lepisto, V. T. Kuokkala, and P. O. Kettunen, *Mater. Sci. Eng.* **81**, 457(1986).

61. H. Neuhauser, *Patterns, Defects and Materials Instabilities*, Eds. D. Walgraef and N.M. Ghoniem (NATO ASI Series E, Applied Sciences, Kluwer Academic Publishers, Dordrecht/Boston/London.) **183**, 241 (1990).

62. H. Neuhauser, *Plastic and Fracture Instabilities in Materials*, Ed. N.M. Ghoniem (ASME Publication, New York) **AMD-200/ MD-57**, 101 (1995).

63. A. Orlova and J. Cadek, *Mater. Sci. Eng.* **77**, 1 (1986).

64. A. S. Argon, F. Prinz, and W. C. Moffat, in *Dislocation Creep in Sub-Grain Forming Pure Metals and Alloys*, Edited by B. Wilshire and D. R. J. Owen (Pineridge, Swansea, 1981), p.1.

65. H. Mughrabi, *Mater. Sci. Eng.* **33**, 207 (1978).

66. C. Laird, P. Charsley, and H. Mughrabi, *Mater. Sci. Eng.* **81**, 433 (1986).

67. S. Takeuchi and A. Argon, *J. Mater. Sci. Eng.* **11**, 1542 (1976).

68. R. Reppich, *J. Mater. Sci.* **6**, 267 (1971).

69. W. G. Johnston and J. J. Gilman, *J. Appl. Phys.* **30**, 129 (1959).

70. H. Huang, N.M. Ghoniem, T. Diaz de la Rubia, M. Rhee, H. Zbib and J. Hirth, *J.* Eng. Mat. Tech., **121, No. 2**, 143 (1999) .

71. A. C. Erringen, *Mechanics of Continua*, **John Wiley & Sons**, New York, p.127 (1967).

72. L. E. Malvern, *Introduction to the Mechanics of a Continuous Medium*, **Prentice-Hall**, New Jersy, (1969).

73. M.O. Peach and J.S. Koehler, *Phys. Rev.*, **80**, 436 (1950).

74. S.D. Gavazza and D.M. Barnett, *J. Mech. Phys. Solids*, **24**, 171 (1976).

75. L. A. Gore, *Determination of the Equilibrium Shapes of Planar Shear Loops in Cubic Crystals,"* Ph.D. Dissertation, Stanford University, 1980.

76. G. Nicolis and I. Prigogine, *Self-Organization in Nonequilibrium Systems*, **John Wiley & Sons**, New York (1977).

77. L. Onsager, *Phys. Rev*, **37**, 405 (1931).

78. J. Lothe and J.P. Hirth, *J. Appl. Phys.*, **38**, 845 (1967).

79. D. Maroudus, *Appl. Phys. Lett.*, **67**, 798 (1995).

80. Z. Suo, *Adv. Appl. Mech.*, **33**, 1 (1996).

81. T.J.R. Hughes, In *Computational Methods for Transient Analysis*, Eds. T. Belytschko and T.J.R. Hughes, North-Holland, p. 67 (1983).

82. S. Amelinckx, The Direct Observation of Dislocations, **Academic Press**, New York, (1964).

83. L.P. Kubin, B. Devincre, and M. Tang, *J. Comp.- Aided Mat. Design*, **5**, 31(1998).

84. E. Kröner, Ergrb. Angew. Math. **5**, 1 (1958).

85. J. M. Burgers, *Proc. Koninkl. Ned. Akad. Wetenschap.*, **42**, 293, (1939).

86. U. Essmann and H. Mughrabi, *Phil. Mag. A*, **40**, 731(1979).

87. B. Tippelt, J. Bretschneider and C. Holste, *Phil. Mag. Lett.* **3**, 161(1996).

88. S.J. Zhou, D. L. Preston, P.S. Lomdahl, and D.M. Beazley, *Science*, **279**, 1525 (1998).

89. S. Takeuchi and K. Maeda, *Acta Metall.*, **25**, 1485 (1977).

90. W. Wasserbach, *Phil. Mag. A*, **53**, 335 (1986).

91. A. Moulin, M. Condat and L.P. Kubin, "Mesosclae Modeling of the Yield point Properties of Silicon Crystals,", *Acta Mater.*, (1999), in the press.

92. W.C. Dash, *J. Appl. Phys.*, **27**, 1193 (1956).

93. N.M. Ghoniem and B. Singh, "Dislocation Dynamics study of the onset of plastic instabilities in irradiated materials," *Proc. of* 20^{th} *RISO Int. Symp. on Mat. Sci.*, 6-10 September (1999).

94. L.Z. Sun, N.M. Ghoniem, B. Singh, and Shih-Hsi Tong, *Phil. Mag.*, submitted, (1999).